Revision 3 - Exploring the effect of lithium on pegmatitic textures – an experimental study

Victoria Maneta[1] and Don R. Baker[1]

[1]Department of Earth and Planetary Sciences, McGill University, 3450 University Street, Montreal QC H3A 0E8, Canada. E-mail: viktoria.maneta@mail.mcgill.ca, don.baker@mcgill.ca

ABSTRACT

The effect of lithium (Li) on the development of pegmatitic textures was evaluated experimentally at H_2O-saturated and H_2O-undersaturated conditions at 500 MPa pressure and temperatures ranging from 400 °C to 800 °C. The addition of ~3700 ppm Li to a starting material of common granitic composition (Lake County obsidian) reduces the crystallization and melting temperatures by approximately 50-70 °C and 200 °C, respectively, and promotes the formation of quartz/feldspar graphic and granophyric intergrowths. The presence of Li in the hydrous granitic system lowers significantly the degree of undercooling needed for the development of graphic and granophyric intergrowths to 85-110 °C in comparison with the Li-free systems where approximately 200 °C of undercooling is necessary. The feldspar crystals developed in Li-bearing samples can incorporate from 150 to 250 ppm Li, assume skeletal and spherulitic morphologies, and exhibit one order of magnitude faster growth rates than crystals in Li-free samples. The results of this study attest to the effectiveness of Li as a fluxing agent and highlight the crucial role it plays in the development of pegmatitic textures, leading to important implications for the conditions of formation of Li-bearing granitic pegmatites.

Keywords: granitic pegmatites, lithium, undercooling, graphic textures, granophyric textures, fluxing agent

INTRODUCTION

Lithium is used in a wide range of applications, the most important of which is lithium-ion rechargeable batteries (Jaskula 2012). The market for lithium-ion rechargeable batteries has expanded significantly during the past years and has come to include electronic devices and hybrid cars, as well as wind and solar energy plants (Grosjean et al. 2012). Pegmatites currently account for 38% of the known global lithium resources and according to recent assessments the mining of Li-bearing pegmatites is predicted to dominate the future markets, since these rocks provide the highest grade ore and enough supplies to cover the increasing demand of lithium (Grosjean et al. 2012, Linnen et al. 2012). Although numerous publications on pegmatites exist in the literature, there are only a few studies that investigate the effect of Li_2O on the granitic system and its implications on the formation of pegmatites (e.g., Vaughan 1964; Wyllie and Tuttle 1964; Gluyk and Trufanova 1977; Stewart 1978; Martin 1983). Considering the forecasted progressive increase in Li consumption and demand in the future, it becomes imperative to obtain a better understanding of the mechanisms involved in the formation of Li-bearing pegmatites.

The genesis of pegmatites has been a matter of debate for many years (e.g., Jahns and Burnham 1969; London et al. 1989; Cerny 1991; London 2005, 2008; Simmons and Webber 2008; Thomas et al. 2012). The most prevalent models agree that pegmatitic textures indicate disequilibrium crystallization that takes place after the temperature has dropped below the liquidus temperature of the system (Fenn 1986; London et al. 1989; Baker and Freda 2001; London 2005). Additionally, the bulk composition of pegmatite-forming melts corresponds to the haplogranitic system enriched in fluxing components such as H_2O, B, F, P, Cl, OH^-, CO_2, HCO_3^-, CO_3^{2-}, SO_4^{2-}, Li, Rb, Cs and Be (Jahns and Burnham 1969; Burnham 1979; Cerny 1991;

London 2008; Thomas et al. 2012). These components reduce the viscosity of the melts and facilitate the diffusion of essential structural elements towards the crystallization front (Hess et al. 1995; Dingwell et al. 1996; Romano et al. 2001; Bartels et al. 2011). Most of these components are incompatible in quartz and feldspar, the early-formed pegmatitic minerals, and become enriched in the residual melt through fractional crystallization (Tuttle and Bowen 1958; Jahns and Burnham 1969; Burnham 1979; London et al. 1989). In addition, the fluxing components reduce crystallization temperatures and enhance the solubility of H_2O in the melt, both of which consequently delay the formation of a separate aqueous phase (Wyllie and Tuttle 1964; Manning 1981; Martin 1983; Johannes and Holtz 1996; Romano et al. 1996; Dingwell et al. 1997; Behrens et al. 2001; Sirbescu and Nabelek 2003; London 2008). The fluxing agents also decrease nucleation density, the number of nuclei that are formed per unit volume, which promotes the formation of fewer but larger crystals, a typical feature encountered in pegmatites (Fenn 1977; London 2005).

London (1992) delineated the criteria that distinguish pegmatites from compositionally similar granites and stressed the necessity for any successful model to be able to explain the most important features of this rock type. Pegmatites are typically coarse-grained rocks, with the size of individual crystals ranging from a few centimeters to over a meter in large pegmatitic bodies. Furthermore, the variability in crystal sizes among different parts of the rock is an important distinguishing feature of pegmatites. In pegmatites that exhibit zoning, the size of crystals increases from the margin to the center, whereas in other cases fine-grained mineral assemblages are encountered between much larger crystals. Heterogeneous and anisotropic textures of mineral assemblages are another characteristic of pegmatites, the most common of which is the graphic intergrowth between quartz and K-feldspar. Radial and skeletal crystal habits as well as layered

and comb structures are also encountered in pegmatites. Individual crystals often exhibit zonation that reflects chemical heterogeneity. The same chemical heterogeneity is also expressed macroscopically in the segregation of the major mineral constituents of pegmatites (quartz, K-feldspar, albite) in almost monomineralic zones. Finally, pegmatites exhibit strong chemical fractionation as several trace elements, such as Li, Rb, Cs, Be, Nb, Ta and REE (Cerny 1991), become enriched - by factors of 10^3 to 10^4 - in comparison with their average concentrations in granites. Chemical fractionation is also developed on a regional scale, where the most distal units of a group of pegmatites are more chemically evolved compared to the ones that are closer to the source granite.

The unique textural characteristics of pegmatites have been reproduced experimentally by several researchers under various conditions (Swanson 1977; Fenn 1986; London et al. 1989; Baker and Freda 2001; and other experimental studies summarized in London 2008). The advantage of experimental studies on the genesis of pegmatites is that they allow control over crucial factors that influence their formation, such as the composition, pressure, temperature, degree of undercooling, and cooling rates, as well as the amount of time that the system remains under the selected conditions. This study investigates the effect of Li on the development of pegmatitic textures under H_2O-saturated and H_2O-undersaturated conditions at 500 MPa and 400-800 °C and evaluates the potential of Li as a fluxing component in pegmatite-forming melts.

EXPERIMENTAL METHODS

Starting material

The starting material selected for the experiments was natural obsidian from Lake County, Oregon (LCO). Table 1 contains the composition of the starting material, analyzed by

electron microprobe analysis (EMPA) at McGill University (from Baker et al. 2002). LCO has a typical granitic composition. Analyses of another sample of LCO performed by ion microprobe (SIMS) at the University of Chicago rendered a Li concentration of 51.9 ppm (from Richter et al. 2003), and the water concentration of LCO was measured to be 0.2% (Harrison and Watson 1983). The starting material was crushed to a fine powder with a grain size of 20 μm using an agate mortar and was subsequently stored in an oven at 120 °C.

As the aim of our study was to recognize any differences in crystal growth between the Li-free and the Li-bearing system, we included crystal seeds in all experiments in order to compensate for any results produced by differences in nucleation. Quartz from the Jucumba Pegmatite District (California), albite from the Amelia County (Virginia) and K-feldspar from Bancroft (Ontario) were added as seeds in most experiments to facilitate nucleation. The crystals were crushed in an agate mortar and then sieved to a grain size between 90 and 106 μm for quartz, and between 106 and 125 μm for albite and K-feldspar.

Addition of Li to the starting material

Our aim is to investigate the effect of a representative, low concentration of Li on the growth of crystals in a pegmatite-forming melt. The Li concentration was chosen so that the system would eventually yield Li-aluminosilicates as crystallization progressed. To this end, a batch of Li-enriched LCO (Li-LCO) was prepared by mixing approximately 2% Li_2CO_3 with LCO powder in an agate mortar for 1 h. A platinum crucible containing the Li-enriched powder was placed in a furnace at 800 °C for 8 h to decarbonate the mixture. Next, the material was melted at 1550 °C for 1 h. The Li-LCO glass produced was crushed to a fine powder and remelted a total of three times at 1550 °C in order to ensure homogenization. Analyses of the

material performed by EMPA confirmed that the homogenization was satisfactory as the maximum standard deviation for major elements was ± 0.3% and for minor elements ± 0.05%. The Li-LCO glass was analyzed for Li with atomic absorption spectrometry (AAS) at McGill University and its concentration was found to be 3712 ppm. The glass was also analyzed by ion microprobe at the Northeast Regional Ion Microprobe Facility (Woods Hole, MA); the maximum standard deviation calculated for Li from SIMS data was ± 1.4%. The composition of Li-LCO is included in Table 1. Comparison of the two compositions shows a shift in the aluminum saturation index from slightly peraluminous for LCO (Al/(Ca+Na+K)=1.06 and Al/(Na+K)=1.10) to slightly peralkaline for the enriched Li-LCO (Al/(Ca+Na+K+Li)=0.85 and Al/(Na+K+Li)=0.88). The Li concentration of the Li-LCO starting material falls within the range of values reported in the literature for various pegmatitic bodies, approximately 5-22000 ppm Li (e.g., Jahns 1953; Vaughan 1964; Wyllie and Tuttle 1964; Stewart 1978; Martin 1983; Cerny 1991; Roda et al. 1995; Maloney et al. 2008; Potter et al. 2009), and was thus considered appropriate for the objective of this study. Additionally, the well-studied, spodumene-bearing Harding pegmatite in New Mexico was reported to contain ~3000 ppm Li (Vaughan 1964), which is consistent with the Li concentration used in our Li-bearing experiments.

Experimental techniques in the piston-cylinder apparatus

The samples were loaded in $Au_{75}Pd_{25}$ capsules, 3 mm in diameter and 9 mm in length. Each experimental sample contained between 3 and 12% distilled H_2O to study the textures formed in both H_2O-undersaturated and H_2O-saturated conditions, 30 mg of the starting material and a total of 0.9 mg quartz, albite and K-feldspar crystal seeds in equal proportions, placed in the capsule in layers in the above order from the bottom to the top of the capsule (Fig. 1). The capsules were subsequently welded closed in a water bath, in order to avoid water loss, weighed

and placed in the oven at 120 °C to dry for at least 2 h. After drying, the capsules were weighed again to check for potential water loss.

In order to test the reproducibility of the results described in this study, replicate experiments were performed. The observations that follow in the experimental results section were typically based on four replicate experiments, ensuring the reliability of the data presented.

The pressure selected for the experiments was 500 MPa and the temperatures varied from 400 to 800 °C. A pressure of 500 MPa was chosen to study the effect of Li on pegmatite-forming melts as it falls within the stability field of spodumene in pegmatites (London and Burt 1982) and agrees with pressure estimates of various pegmatitic bodies (e.g., Lentz and Fowler 1992; Partington et al. 1995). Furthermore, this pressure is well-calibrated in our piston-cylinder apparatus (Holloway and Wood 1988; Baker 2004). The duration of the runs ranged from 0 to 100 h. The pressure and heating/cooling rates were kept constant in all the runs, while the temperature, composition of the samples and duration of the experiments were treated as variables. Additionally, the crystallization of unmodified LCO and enriched Li-LCO, with or without the presence of quartz, albite and K-feldspar crystal seeds, was studied.

All experiments were conducted in the piston-cylinder apparatus using 3/4-in. NaCl-Pyrex glass-graphite-crushable alumina assemblies (Hudon et al. 1994). Temperatures in the runs were measured with tungsten-rhenium thermocouples ($W_{26}Re_{74}$-W_5Re_{95}). The vertical thermal gradient in the center of the assembly was estimated to less than 5 °C over 4 mm for the temperature range used in this study (Hudon et al. 1994). The piston-cylinder was calibrated at 500 MPa by water solubility in albite melt (Baker 2004). Each assembly was loaded in the piston-cylinder and heated at a rate of 100 °C/min to 1000 °C and 550 MPa where it remained

for 1 h to allow melting of the starting glasses. Then, the assembly was cooled at 50 °C/min to the desired temperature and 500 MPa where it remained for 0, 50 or 100 h. At the end of the runs the samples were rapidly quenched isobarically to ambient temperatures. The selection of the duration of the experiments was based on cooling models applied to the crystallization of pegmatitic dikes (Webber et al. 1999), according to which approximately 5 days was enough time for the 1 m thick Himalaya dike (California) to have cooled to a temperature of <550 °C. Additionally, previous experimental studies performed on a hydrous haplogranitic system reproduced pegmatitic textures in 100 h long experiments at 500 MPa (Baker and Freda 2001).

Analytical conditions for Electron Microprobe Analysis

The experimental capsules were mounted longitudinally in epoxy, ground open approximately half-way through the capsule, polished and carbon-coated for analysis by the electron microprobe. The imaging and analyses were performed at McGill University on a JEOL 8900 electron microprobe using a beam between 1 and 10 μm in diameter for crystallized sections of the capsules, depending on the size of the crystals and textures analyzed, and 50 μm for analyses of the glass. The elements analyzed in crystals were Si, Ti, Al, Fe, Mn, Mg, Ca, Na and K; counting times of 20 s on the peaks and 10 s on the background, 15 kV acceleration voltage and a beam current of 20 nA were used. The electron microprobe was calibrated for analysis of the crystals using orthoclase (Si, Al, K), rutile (Ti), hematite (Fe), spessartine (Mn), diopside (Mg), anorthite (Ca) and albite (Na) as standards. The elements analyzed in the glass were Si, Ti, Al, Fe, Mn, Mg, Ca, Na, K and F. The counting times for all elements except Na were the same as for the crystals. In order to minimize Na loss during analysis of the hydrous glasses (Morgan & London 1996), the counting times for Na on the peaks and the background were selected as 15 and 7.5 s, respectively. The acceleration voltage was kept at 15 kV and a

beam current of 8 nA was used. The standards used for glass analysis were rhyolite (Si, Al), basalt (Ti, Fe, Mg, Ca), spessartine (Mn), albite (Na), orthoclase (K) and fluorite (F).

Analytical conditions for Secondary Ion Mass Spectrometry

The Li concentrations of the samples were analyzed with SIMS at the Northeast Regional Ion Microprobe Facility, Woods Hole Oceanographic Institution, using a CAMECA IMS 1280 secondary ion mass spectrometer. The capsules were mounted in 1-in. round mounts, polished and gold-coated. The isotopes ^{7}Li and ^{30}Si were chosen for analysis and the ratio ^{7}Li/^{30}Si was used to calculate Li concentrations. Pre-sputtering was set to 300 s and the output intensity was detected by an electron multiplier. An average of 20 cycles was obtained from each spot analysis which was performed with a 15 μm spot beam. Two glasses with known Li-concentrations, 3712 ppm and 4493 ppm, were used as standards for the crystals and the glass in the capsules. Spot analyses on the samples were performed with two beams, an initial one of 5 nA combined with a final one of 1 nA for low Li concentrations and a 5 nA beam combined with a 300 pA one for the higher concentrations of Li. Analyses on the two standard glasses provided good results which were in agreement with data obtained with AAS. Analyses on the crystals, however, were possibly affected by matrix effects (Macfarlane and Shimizu 1991), since a glass was used as the standard instead of crystals. Thus, the Li concentrations calculated for the crystals should be considered only qualitative. Nevertheless, the analyses on crystals can be used in combination with the Li content of the glasses in order to assess the partitioning of Li between the melt and crystals as well as to confirm the identity of Li-aluminosilicate minerals formed in the experiments.

EXPERIMENTAL RESULTS

The conditions of the runs and the phases developed in the experiments are summarized in Table 2. In the description that follows, the samples are grouped together according to the conditions of the experiments, starting with the ones performed with the unmodified LCO starting material and proceeding to experiments with the enriched Li-LCO. The scarcity of experimental data in the literature regarding the effect of Li on the granitic system (Vaughan 1964; Wyllie and Tuttle 1964; Glyuk and Trufanova 1977; Stewart 1978; Martin 1983) makes a comparison between Li-free and Li-bearing experiments necessary, with emphasis on changes on the liquidus and the solidus temperatures brought about by the addition of Li. Furthermore, since this is the first study that provides textural information on the granitic system enriched with Li, it is essential to include detailed observations on the crystallizing phases, the crystal morphology and the pegmatitic intergrowths developed in the runs.

The use of the terms "granophyric" and "graphic" in the text and the backscattered images follows the description of Barker (1970) and is based on the size of the textures and the shape of the crystals. Granophyric is applied to submicroscopic quartz-feldspar intergrowths, where quartz forms vermicular or cuneiform crystals that usually do not exceed 1-3 μm in the host feldspar. Graphic is used for submicroscopic to millimeter size quartz-feldspar intergrowths, where quartz forms cuneiform crystals in parallel arrangement, usually 10-20 μm in size, or an order of magnitude larger than the granophyric crystals.

Li-free experiments

Evaluating the liquidus temperature of the Li-free system under H_2O-saturated and H_2O-undersaturated conditions. In order to generate the starting material for the melting experiments described in this section, a 2 week long crystallization experiment was conducted

using a hydrated core of LCO glass in a cold-seal pressure vessel at 50 MPa and 805 ±5 °C. Optical examination of the run products from the crystallization experiment, using an immersion oil with 1.564 refractive index, showed that it contained approximately 20% crystals, whereas the remainder of the capsule was occupied by glass and vesicles. The crystal phases included a green prismatic clinopyroxene, with higher refractive index than the glass, as well as quartz and feldspar crystals that often formed spherulitic intergrowths. The H_2O content of the partly crystalline LCO was calculated at 3% using the model by Papale (1997). This partly crystalline LCO was ground to powder, divided in eight capsules with 6% and 20% total H_2O and used in four 50 h experiments in the piston-cylinder apparatus at 500 MPa and 680, 720, 760 and 800 °C in order to constrain the liquidus temperature of the Li-free granitic system under H_2O-undersaturated and H_2O-saturated conditions. At 680 °C the H_2O-saturated capsule contained approximately 10% clinopyroxene, quartz and feldspar crystals, whereas the remainder was occupied by glass and vesicles. The same crystal phases were observed in the H_2O-undersaturated sample, but the amount of crystallization was 30% and there were no vesicles. Quartz and feldspar usually formed spherulitic intergrowths in both cases. At 720 °C quartz and feldspar melted and only clinopyroxene was observed in the H_2O-saturated sample, whereas in the H_2O-undersaturated capsule all three phases were still present, but at less than 5% abundance. At 760 °C, the H_2O-saturated capsule contained only glass and vesicles, whereas in the H_2O-undersaturated run a few clinopyroxene crystals and traces of quartz were observed. At 800 °C all crystals melted in both capsules. From these experiments, we estimated the position of the liquidus of the Li-free system at 740 ±20 °C and 780 ±20 °C for the H_2O-saturated and H_2O-undersaturated runs, respectively. Similarly, the quartz-feldspar saturation curve was placed at 700 ±20 °C for the H_2O-saturated and at 740 ±20 °C for the H_2O-undersaturated system.

Furthermore, we compared the results from the experiments with the liquidus temperatures calculated by rhyolite-MELTS (Gualda et al. 2012) and we found that the calculated values agreed with the temperature range estimated from the experimental results, thus confirming the validity of the data. More specifically, the calculated liquidus was at 737 °C for the H_2O-saturated and at 795 °C for the H_2O-undersaturated system, with trace amounts of quartz as the liquidus phase in both cases. Trace amounts of feldspar were first formed at 719 and 784 °C, respectively, but the crystals approached 5% at 716 and 744 °C instead. For the sake of simplicity, we used the values 740 and 780 °C as the liquidi temperatures for the Li-free H_2O-saturated and H_2O-undersaturated systems, respectively, in the following sections.

Effect of varying run duration. The Li-free experiments were conducted at 500 MPa pressure and 600 °C temperature using the original LCO as the starting material, 12% H_2O and quartz, albite and K-feldspar crystal seeds. All experiments followed the heating and cooling protocol described above. The duration of the experiments varied between 0, 50 and 100 h. The capsules from the 0 h run at 600 °C final temperature (PGT 5 and 6) contained only glass and numerous vesicles (from 1 to 100 μm in diameter), indicating that the samples with 12% H_2O were already H_2O-saturated from the beginning of crystallization, as expected (cf. Baker and Alletti 2012). No crystal seeds and no new crystals were observed in the two dimensional sections examined, although based upon other experiments (discussed below) we believe that crystal seeds still existed in the run products. These experiments indicate that despite the presence of crystal seeds, more time is necessary for crystallization at the conditions investigated. They also show that the crystals formed in all other experiments that follow are neither quench crystals nor crystals grown during the high-temperature homogenization step.

Apart from glass and vesicles, the capsules from the 50 h run (PGT 3 and 4) also contained small anhedral to subhedral clinopyroxene crystals (maximum length of 5 μm) and bladed crystals of a Ca-rich silicate mineral (maximum length of 100 μm). The bladed morphology of the mineral, with a maximum width of 1 μm, made analysis with EMPA very difficult and accurate results were not obtained for these samples. The same phase was encountered in Li-bearing samples as well, forming larger crystals which provided better analytical results, so discussion of the composition of the bladed Ca-silicate mineral is postponed until the section describing the Li-bearing runs. A few quartz crystals that were found close to the bottom of the capsules in both samples were identified as remnants of the crystal seeds due to cracks in them, the dissolution features observed, and because the size of the crystals was similar to that of the original seeds (~100 μm). New vermicular growth of quartz around, or close to, the seeds was observed in both samples (maximum length of 30 μm). A few K-feldspar crystals with skeletal morphology were formed close to the top of PGT3 (maximum length of 40 μm). The position of the newly grown crystals in the samples corresponded to the original position of the crystal seeds in the capsules (bottom for quartz and top for K-feldspar), which suggests that in those parts of the capsules the melt was enriched in the essential structural elements for the newly grown minerals after the seeds were partly or completely dissolved (Evensen 2001).

Capsules PGT 1, 2, 27 and 28 remained at 500 MPa and 600 °C for 100 h. Figure 2 shows representative backscattered images of the samples obtained with EMPA. The capsules contained mainly glass and vesicles (Fig. 2a), as well as a few anhedral clinopyroxene crystals and the bladed Ca-rich silicate phase (Fig. 2b), in agreement with the 50 h experiments. A very small fraction of the area observed, estimated at less than 2% using image analysis (ImageJ) on the backscattered images, was occupied by individual K-feldspar crystals that exhibited skeletal

morphology (Fig. 2b). In some cases in the same sample the K-feldspar grew from the walls of the capsules toward the center (Fig. 2a), whereas in others it formed isolated crystals surrounded by melt (Fig. 2b). The minimum growth rate of the feldspar was calculated by dividing the maximum length of the crystals with the duration of the experiments, making the assumption that the growth started immediately after the runs reached the temperature of 600 °C. The size of the crystals ranged between 10 and 500 μm and the minimum growth rates were from $10^{-10.6}$ to $10^{-9.2}$ m/s. The average composition of the K-feldspars is shown in Table 3. Analyses of the glass are included in Table 4. In two of the samples remnants of the quartz seeds were found at the bottom of the capsules surrounded by newly formed vermicular quartz with the same characteristics as in the 50 h experiments. Importantly, no pegmatitic textures were formed in any of the Li-free samples.

Li-bearing experiments

For the Li-bearing experiments (3712 ppm Li) we used Li-LCO as the starting material, with or without the addition of quartz, albite and K-feldspar crystal seeds, and 3-12% H_2O. A pressure of 500 MPa was used in all the runs and the temperature ranged from 400 to 800 °C. The duration of the runs was 100 h except for two experiments at 600 °C which were performed for 0 and 50 h for comparison with the corresponding Li-free experiments.

Evaluating the degree of undercooling under H_2O-saturated and H_2O-undersaturated conditions. In order to evaluate the degree of undercooling in the Li-bearing experiments, we needed to constrain the liquidus and solidus temperatures of the Li-enriched granitic system. Two capsules loaded with Li-LCO powder and ~3% H_2O were allowed to crystallize at 500 °C and 500 MPa for 100 h. At the end of the run, the capsules were opened and

the material formed was examined optically under the microscope for the presence of glass and crystals using an immersion oil with 1.564 refractive index. The phases identified were individual feldspar crystals, spherulitic quartz-feldspar intergrowths and a bladed green mineral with a higher refractive index than the immersion oil, possibly a clinopyroxene. The amount of glass present was estimated at <10%. From this experiment, we were able to constrain the solidus temperature to under 500 °C. The material formed in this run was ground to powder, divided in four capsules with approximately 8% and 18% total H_2O and used in two experiments at 500 MPa in order to determine the liquidus temperatures under H_2O-saturated and H_2O-undersaturated conditions. The duration of both experiments was 50 h and the temperatures selected were 680 and 700 °C, respectively. Again, the run products were examined optically for the presence of glass and crystals. At 680 °C both capsules contained mostly glass. In the H_2O-saturated capsule <5% clinopyroxene and feldspar crystals were observed, while the H_2O-undersaturated sample contained <10% of the same crystalline phases including quartz. At 700 °C the crystals melted completely in the H_2O-saturated capsule, whereas <5% of the above crystal phases remained in the H_2O-undersaturated sample. From these experiments, we estimated the position of the liquidus of the Li-enriched system at 690±10 and 710 ±10 °C for the H_2O-saturated and H_2O-undersaturated runs, respectively. The quartz-feldspar saturation curve coincided with the liquidus in this system.

Five experiments with Li-LCO and ~6-12% H_2O were conducted at 500 MPa, using the same heating and cooling protocol as the Li-free runs, in order to confirm the position of the liquidus as well as estimate the degree of undercooling that relates to the formation of pegmatitic textures under H_2O-undersaturated and H_2O-saturated conditions. The temperatures selected for these experiments were 800, 750, 700, 650 and 625 °C, and the duration was 100 h. The runs at

800, 750 and 700 °C contained only glass and vesicles and no crystals were observed in the two dimensional sections examined. The vesicles in the samples with ~6% H_2O were fewer and smaller in size than the ones developed in the capsules with ~12% H_2O (maximum diameter of 30 and 100 μm, respectively), demonstrating that the samples with 6% H_2O are initially H_2O-undersaturated as expected (cf. Baker and Alletti 2012). The runs at 650 °C started developing very few small clinopyroxene crystals, less than 10 μm in size, whereas the remainder of the capsules was filled with glass and vesicles. The vesicles ranged from 1-100 μm and <1-20 μm in the H_2O-saturated and H_2O-undersaturated samples, respectively. At the bottom of the H_2O-undersaturated capsule, remnants of quartz seeds were observed with new vermicular quartz overgrowth around them (20 μm maximum length). None of these runs developed any feldspar crystals.

Samples PGT 57 (H_2O-saturated) and 58 (H_2O-undersaturated) performed at 625 °C present the most interesting results among the samples described in this section. Figure 3 includes representative backscattered images of the crystals and textures formed in the runs. Both capsules contained glass and vesicles, analogous with the runs at 650 °C. PGT 57 developed numerous subhedral to euhedral clinopyroxene crystals, from 1 to 30 μm maximum length, as well as the Ca-silicate phase which formed bladed crystals ranging in length from 5 to 200 μm (Fig. 3a). The coarse size of the crystals in this sample as well as the lack of other crystal phases facilitated EMPA analysis and helped obtain more precise data for these two minerals. Average analyses and cation calculations are included in Table 3. The composition of the clinopyroxene seems to fall into the aegirine-augite series with an average chemical formula $(K_{0.005},Na_{0.172},Ca_{0.748},Fe^{3+}_{0.042})(Al_{0.070},Fe^{2+}_{0.193},Fe^{3+}_{0.001},Mn_{0.100},Mg_{0.594})Si_{2.022}O_6$. Since the melt becomes slightly peralkaline with the addition of Li in the system, as previously mentioned,

formation of an alkali pyroxene is not unexpected. The bladed Ca-silicate phase that appeared to develop after the clinopyroxene was more difficult to identify. The composition that best matched the analytical data was that of truscottite, a hydrous calcium silicate mineral with the chemical formula $Ca_{14}(Si_{24}O_{58})(OH)_8 \bullet xH_2O$ (Lachowski et al. 1979). The crystals had an average Ca:Si ratio of 0.74, which falls within the corresponding range reported for truscottite (0.5-0.75). Truscottite can also accommodate up to 1.4 atoms of Al and 0.5 atoms of K in the structure, as well as Mn (Lachowski et al. 1979), which is consistent with the analytical data obtained for the Ca-silicate mineral formed in the experiments. No quartz or feldspar crystals were found in this run. The crystal fraction was estimated at less than 0.5%.

In the H_2O-undersaturated sample PGT 58 numerous clinopyroxene and Ca-silicate crystals were formed (white crystals in Fig. 3b-e) with similar size and average chemical composition as in H_2O-undersaturated PGT 57. In this sample, however, K-feldspar and quartz crystals were also developed, increasing the amount of crystallization to approximately 22%, as calculated with ImageJ. K-feldspar formed skeletal and tabular crystals (1-200 μm maximum length) that nucleated in the melt (Fig. 3b, top left, and f) or grew from the rims of the capsule towards the center (Fig. 3d, top left), as well as extensive spherulites (~2000 μm maximum length). Quartz was typically found in graphic and granophyric intergrowths with K-feldspar (Fig. 3b-f). The length of the graphic quartz rods varied from 1 to 20 μm (Fig. 3b and c), whereas in the granophyric intergrowths quartz crystals reached 3 μm maximum length (Fig. 3b). The minimum growth rates calculated for quartz crystals varied from $10^{-11.6}$ to $10^{-10.8}$ m/s for the granophyric textures and from $10^{-10.8}$ to $10^{-10.2}$ m/s for graphic quartz, showing a gradual increase in the growth rate of quartz as the texture changes from granophyric to graphic towards the edge of the crystallization front. The degree of undercooling reached at the onset of the formation of

383 graphic and granophyric intergrowths in the H_2O-undersaturated samples was estimated at about
384 85 °C.

385 The relationship between the graphic and granophyric textures and the sequence of
386 crystallization could be observed in several cases in PGT 58 (Fig. 3d-f). Individual K-feldspar
387 crystals with skeletal or tabular morphology appear to be forming first followed by granophyric
388 intergrowths between quartz and K-feldspar. Coarser, graphic quartz-feldspar textures were
389 developed at the edge of the crystallization front, usually surrounding the granophyric
390 intergrowths. In order to investigate compositional differences between the graphic and
391 granophyric textures (Barker 1970; Morgan and London 2012), selected traverses were analyzed
392 by the electron microprobe. The analyses were performed using a 1 μm beam and a 2 μm step.
393 The data acquired from each traverse were averaged and recalculated as normative CIPW weight
394 percent of quartz, albite and K-feldspar end-members following the method developed by Cross
395 et al. (1902). The results are presented in Figure 4 in a Qz-Ab-Or ternary plot. The two types of
396 textures in this sample appear to be compositionally similar, with the average CIPW components
397 approaching the value $Qz_{27}Ab_{19}Or_{52}An_2$ reported for graphic granite in Barker (1970). The
398 granophyric textures are more enriched in Or than in Qz and Ab components compared with the
399 average $Qz_{36}Ab_{33}Or_{28}An_3$ value stated for granophyre in Barker (1970). The fact that both types
400 of textures have very similar compositions in this sample suggests that the graphic intergrowths
401 are probably the evolution of the granophyric textures through time as crystallization progresses.
402 It is plausible that the textural differences could be due to local changes in the rheological
403 properties of the melt at the edge of the crystallization front, as shown by the increase in growth
404 rate measured for quartz in both types of intergrowths. More details are provided in the
405 discussion.

406 **Importance of crystal seeds.** The presence of crystal seeds has been shown to facilitate
407 nucleation in 100 h long experiments performed under conditions similar to those used in this
408 study (Baker and Freda 2001). In order to verify the necessity for crystal seeds for 100 h long
409 runs, we conducted two experiments with Li-LCO, ~6-12% H_2O and no seeds at 500 MPa and
410 600 °C. All four capsules from these runs contained glass and vesicles, while the only minerals
411 formed were a few subhedral to euhedral clinopyroxene crystals and the bladed Ca-rich mineral
412 phase. No quartz or feldspar crystals were developed in the runs, contrary to seeded experiments
413 performed under exactly the same conditions (see Table 2 and the following subsection on the
414 effect of temperature).

415 **Effect of varying run duration.** In order to highlight the effect of Li on the pegmatite-
416 forming melt, 0, 50 and 100 h long experiments were conducted with Li-LCO and ~12% H_2O at
417 500 MPa and 600 °C, following the same method described in the Li-free experiments section.
418 The run products from the 0 and 50 h experiments were similar to the corresponding Li-free
419 samples. In the 0 time samples (PGT 13 and 14), only glass and vesicles were observed, whereas
420 the capsules from the 50 h run (PGT 25 and 26) also contained a few small anhedral
421 clinopyroxene crystals and the bladed Ca-rich silicate phase developed in the Li-free runs as
422 well. We noted that at the top of PGT 26 very few skeletal K-feldspar crystals were formed, with
423 a maximum length of 100 μm, whereas no remnants of quartz seeds or new quartz crystals were
424 observed in the Li-bearing samples.

425 However, in the 100 h experiments, striking differences between the Li-free and the Li-
426 bearing runs were observed. The amount of crystallization, as estimated with ImageJ, reached 12
427 to 30% in the Li-bearing experiments, in contrast with less than 2% measured in the Li-free ones.
428 The K-feldspar crystals reached 900 μm in size at a growth rate of $10^{-8.4}$ m/s, almost one order of

magnitude faster than the K-feldspar crystals in the Li-free capsules. In addition, quartz was also present in the Li-bearing samples, developing graphic and granophyric intergrowths with K-feldspar crystals, both characteristic textures encountered in pegmatites. A more detailed description as well as representative images of the 100 h experiments at 600 °C follows in the next subsection on the effect of varying temperature and water content.

Effect of varying temperature and water content. After observing the formation of pegmatitic textures in H_2O-undersaturated, Li-bearing samples at 625 °C and 500 MPa, we investigated the effect of adding different amounts of water in the capsules at progressively lower temperatures, starting at 600 °C and moving towards the solidus.

600 °C. Four samples (PGT 15, 16, 33 and 34) with Li-LCO and ~12% H_2O were used in two experimental runs at 600 °C for 100 h. Backscattered images of the crystals and the textures obtained with EMPA are shown in Figure 5. The amount of crystallization was estimated at 12 to 30% with ImageJ, while the remainder of the capsules was occupied by glass and vesicles (1 to 150 μm in size). Most of the largest vesicles were concentrated at the edge of the crystallization front (Fig. 5a, c and d). Small anhedral to subhedral clinopyroxene crystals and the bladed Ca-rich silicate mineral were also present (white crystals in Fig. 5b and c). All four samples share impressively similar characteristics. The majority of the crystals formed were K-feldspar that exhibit skeletal and spherulitic morphologies. Most K-feldspar crystals started on the walls of the capsules and grew toward the center (Fig. 5d). Few individual K-feldspar crystals formed isolated skeletal to tabular crystals or clusters of crystals surrounded by melt (at the edge of the crystallization front in Fig. 5a and d). The size of the crystals ranged from 1 to 900 μm and their average composition is included in Table 3. Note that the K-feldspar formed in Li-bearing samples incorporated 181 ppm Li, which is approximately two orders of magnitude more Li than

452 the feldspar crystallized in the Li-free experiments conducted under the same conditions (7 ppm
453 Li) (Table 3). Some K-feldspar crystals at the edge of the crystallization front developed more
454 Na-rich sections (Fig. 5d). Comparison of the Li content in the K-feldspar (Table 3) and the glass
455 (Table 4), demonstrates that only a small percentage of Li was incorporated in the feldspar
456 structure with the remainder preferentially partitioning in the melt. The minimum growth rates
457 ranged from $10^{-11.2}$ m/s for small isolated skeletal crystals to $10^{-8.4}$ m/s for the larger skeletal
458 crystals and most of the spherulites. Quartz crystals were developed in the Li-bearing samples as
459 well, ranging in size from 1 to 10 μm (Table 3). The quartz was always found in heterogeneous
460 textures with K-feldspar.

461 The most striking textures generated in all four Li-bearing samples are the graphic and
462 granophyric intergrowths between quartz and K-feldspar. The degree of undercooling necessary
463 for the development of the graphic and granophyric textures in the H_2O-saturated samples was
464 estimated at 90 °C. The graphic intergrowths were developed in the host feldspar filling skeletal
465 crystals with quartz that assumed cuneiform morphology. In the granophyric textures quartz
466 exhibited vermicular morphology and usually occupied the edges of the skeletal K-feldspar
467 crystals. The transition from granophyric to graphic textures discussed in the H_2O-undersaturated
468 experiment at 625 °C was not observed in these samples and the relationship between the two
469 types of intergrowth is not clear. The composition of representative graphic and granophyric
470 textures along analytical traverses recalculated as normative CIPW weight percent for Qz-Ab-Or
471 components is presented in Figure 4 on a ternary Qz-Ab-Or plot. The analyses were performed
472 using a beam diameter between 1 and 10 μm, with a step between 2 and 30 μm, depending on
473 the coarseness of the intergrowths and the area they covered. The granophyric textures formed in
474 these samples are compositionally closer to graphic granite $Qz_{27}Ab_{19}Or_{52}An_2$ as described in

Barker (1970). The graphic textures, however, appear more enriched in Or and depleted in Qz and Ab components compared to graphic granite in Barker (1970).

Four samples (PGT 17, 18, 19 and 20) with ~6% H_2O were used in two experiments at 600 °C for 100 h. Figure 6 contains backscattered images of the textures developed in the capsules. In these experiments a significant fraction of each capsule was crystallized, between 31 and 65% as estimated with ImageJ, whereas the remainder was occupied by glass and vesicles. The size of the vesicles ranged from 1 to 100 μm, with the vast majority of the largest vesicles concentrating around extensive K-feldspar spherulites (Fig. 6a and b). The size of the vesicles indicates that the originally H_2O-undersaturated melt reached saturation as crystallization progressed, leading to the separation of an aqueous phase that seems to occur at the crystallization front. Anhedral to subhedral clinopyroxenes and bladed Ca-silicate crystals were also formed in the capsules (white crystals in Fig. 6b, c and d). The K-feldspar spherulites grew from the walls toward the center of the capsules (Fig. 6a) or crystallized independently in the melt. Individual skeletal to tabular K-feldspar crystals were also found, but were typically fewer in number or very small in size (Fig. 6b, top). The size of the K-feldspar varied from 1 to 50 μm for the isolated skeletal crystals and from 100 to 1100 μm for the spherulites. Representative analyses of K-feldspar crystals are included in Table 3. Li concentrations were not obtained due to the small size of the individual crystals. Analyses of the glass in Table 4 show that the Li content has almost doubled in relation to the glass from the runs with 12% H_2O. Minimum growth rates calculated for K-feldspar ranged between $10^{-10.8}$ m/s for the smaller isolated crystals and $10^{-8.2}$ m/s for the larger skeletal crystals and the spherulites. It is essential to note that the K-feldspar crystals evidently coarsened in size towards the edges of the spherulites as crystallization progressed (Fig. 6a and d, top), an observation that can be seen in natural

pegmatites as well (London 1992). Additionally, at the edges of the spherulites, the feldspars developed sections that are notably more Na-rich (Fig. 6b and c), approaching the composition of end-member albite (Table 3). Quartz crystals, which ranged in size from <1 to 10 μm, were typically found as intergrowths with K-feldspar (dark grey to black crystals among K-feldspar in Fig. 6b-d). The same sequence of crystallization, starting with K-feldspar to K-feldspar-quartz intergrowths and finally to albite was previously seen in experiments at 200 MPa and various degrees of undercooling (Evensen 2001).

Graphic intergrowths between quartz and K-feldspar were developed either within the spherulites or filling skeletal K-feldspar crystals that grew from the walls of the capsules (Fig. 6c and d). Granophyric textures with quartz and K-feldspar usually occupied the edges of the spherulites or surrounded the skeletal crystals that grew from the walls of the capsules (Fig. 6c). Average analyses of graphic and granophyric textures along traverses obtained with EMPA are included in the ternary diagram in Figure 4. The composition of the textures analyzed in these samples approaches the average Qz-Ab-Or values reported in Barker (1970) for granophyre ($Qz_{36}Ab_{33}Or_{28}An_3$) and graphic granite ($Qz_{27}Ab_{19}Or_{52}An_2$). However, in the Li-enriched and H_2O-undersaturated system under study, the graphic textures formed appear more Ab-rich and Qz-poor compared to the graphic granite in Barker (1970). Similarly, the granophyric intergrowths are enriched in Or and depleted in Qz and Ab compared to Barker (1970).

Three capsules (PGT 30, 31 and 32) with ~3% H_2O were used in two experiments at 600 °C for 100 h. Representative backscattered images of these samples can be seen in Figure 7. Crystallization, as estimated with ImageJ, varied from 53 to 80%. The remaining fraction of the capsules was filled with glass and vesicles (1 to 100 μm in diameter), the largest of which surrounded the spherulites (Fig. 7a and b). The size and distribution of the vesicles in the

capsules suggest that the melt was initially H_2O-undersaturated and became H_2O-saturated as crystallization progressed. A few anhedral to subhedral clinopyroxene crystals as well as the Ca-silicate bladed crystals were formed in the capsules (white crystals in Fig. 7c and d) among individual skeletal to tabular K-feldspar crystals (1 to 50 μm maximum length) and extensive K-feldspar spherulites (80 to 1600 μm in diameter) (Fig. 7a, b and d). The spherulites seemed to be growing from the walls of the capsules toward the center (Fig. 7a, top and bottom, and b, top right), whereas in other cases they nucleated from the melt and grew radially (Fig. 7a, right and bottom left, and d). The edges of the spherulites developed coarser crystals that consist of K-feldspar (Fig. 7b and c) as well as Na-feldspar (Fig. 7c). The smaller skeletal and tabular K-feldspar crystals usually grew in the melt pools (Fig. 7a, middle). Minimum growth rates calculated ranged from $10^{-11.2}$ to $10^{-8.4}$ m/s for the individual skeletal and tabular crystals and the spherulites, respectively. Graphic and granophyric textures between quartz and K-feldspar, or in a few cases Na-feldspar at the edge of the crystallization front, filled parts of the spherulites in these samples (Fig. 7d). The Li concentration of the glass formed in these experiments reached the highest value measured in this study, 12052 ppm (Table 4), but no Li-rich minerals were observed. This observation strongly suggests that feldspar and quartz incorporate only small amounts of Li, whereas Li preferentially concentrates in the residual melt.

In agreement with the H_2O-saturated runs, the H_2O-undersaturated experiments also suggest that the enrichment of the system with Li leads to the formation of characteristic pegmatitic features, such as the coarsening of the crystals towards the edge of the crystallization front as well as the graphic and granophyric textures between quartz and K-feldspar.

500 °C. Capsules PGT 60 and 59, with ~6 and 12% H_2O, respectively, were used in one experiment at 500 °C for 100 h. Figure 8 includes backscattered images of the samples. The

544 amount of residual melt in the capsules was estimated with ImageJ at approximately 12% for the
545 H_2O-saturated sample (PGT 59) and at close to 7% for the initially H_2O-undersaturated run (PGT
546 60). The Li content of the glass in PGT 59 was measured at 5927 ppm (Table 4). The remainder
547 of the capsules was occupied by crystals and vesicles. The vesicles in both capsules varied in
548 size from 1 to 1200 μm in diameter. In the H_2O-saturated run, a large vesicle located at the top of
549 the capsule occupied almost 1/3 of the total area (Fig. 8a), whereas in the initially H_2O-
550 undersaturated run the crystals covered more area than the vesicles. A separate aqueous phase
551 was formed in both cases, which is expected at this very advanced stage of crystallization, just
552 above the solidus of the system under study.

553 K-feldspar, albite and quartz crystals developed almost monomineralic zones as
554 crystallization progressed. K-feldspar seemed to be crystallizing first in both samples, followed
555 by albite and quartz (Fig. 8a and c). Small anhedral clinopyroxene crystals and the bladed Ca-
556 silicate phase were also present (white crystals in Fig. 8b). The feldspars ranged in size from 20
557 to 150 μm, whereas the quartz zones reached a maximum width of 80 μm. The feldspars
558 exhibited skeletal morphology and usually radiated from the walls of the capsules toward the
559 center (Fig. 8c, top). At the edge of the crystallization front, they formed tabular crystals with
560 separate K-rich and Na-rich sectors developing on the same crystal (Fig. 8b). Quartz was found
561 in graphic and granophyric intergrowths with the feldspars (Fig. 8d), but subhedral crystals were
562 also formed in the quartz zones close to the melt pools (Fig. 8c).

563 As crystallization progressed, a Li-aluminosilicate mineral started developing from the
564 Li-bearing residual melt (Fig. 8b), which explains the relatively low Li concentration measured
565 in the glass in comparison with the more elevated Li values that would be expected in the
566 residual melt from runs just above the solidus. The crystals were anhedral to subhedral ranging in

size from 10 to 50 μm. The composition of the crystals can be seen in Table 3. Both petalite ($LiAlSi_4O_{10}$) and virgilite ($Li_{0.5}Al_{0.5}Si_{2.5}O_6$) are considered plausible potential matches for the Li-aluminosilicate after calculation of the cations based on 10 and 6 oxygen atoms, respectively. Virgilite seems to approach the composition more closely, so only that calculation is included in Table 3. The low Li concentrations measured in the crystals by SIMS (2.01% Li_2O), in comparison with the values found in the literature for virgilite (~4% Li_2O), are attributed to the matrix effect mentioned in the experimental methods section above.

400 °C. Four capsules (PGT 51, 52, 53 and 54) with Li-LCO, crystal seeds, and ~6 or 12% H_2O were used in two experiments at 400 °C for 100 h. Representative backscattered images of the samples are shown in Figure 9. At 400 °C all four capsules were fully crystallized and no glass was found. In the H_2O-saturated runs (PGT 51 and 52) the aqueous phase occupied approximately 1/2 of the capsules, whereas in the initially H_2O-undersaturated runs (PGT 53 and 54) an intricate network was formed between the aqueous phase and very fine-grained crystal textures. Combining the information acquired from the 500 and 400 °C experiments with the data from the crystallization experiment at 500 °C, we estimate that the solidus of the Li-enriched system lies at about 450±50 °C.

Small anhedral clinopyroxene crystals and the bladed Ca-silicate mineral were found in all the capsules. In the H_2O-saturated runs, crystallization took place in several small areas in the capsules where K-feldspar, albite and quartz developed intricate successive zones (Fig. 9b and c). The crystallized clusters appeared to radiate from the K-feldspar center, usually through a more Na-rich feldspar zone and finally quartz next to the aqueous phase that surrounded the clusters (Fig. 9b). The width of each zone was 100 to 200 μm on average, but the proportions of the minerals that comprised the zones sometimes varied among the different clusters. The

feldspars formed anhedral crystals or assumed skeletal morphology (Fig. 9c), whereas quartz formed subhedral crystals close to the edge of the crystallization front (Fig. 9b and c). Graphic intergrowths between K-feldspar and quartz were sometimes developed in the center of the clusters, but they were finer than the textures described in the experiments at 600 °C and not as common. Similar clusters and zones seemed to form in the initially H_2O-undersaturated runs as well, but they were much smaller in size (50 μm maximum width).

Anhedral crystals of the Li-aluminosilicate mineral with a maximum length of 200 μm were formed at the edge of the crystallization front (Fig. 9a and d). They seemed to be the last product of crystallization since they typically followed quartz and were always surrounded by the aqueous phase (Fig. 9d). The composition of this mineral (Table 3) approaches that of virgilite although petalite could also be possible, as discussed above.

Growth Rates

The skeletal and spherulitic morphologies of the K-feldspar crystals formed in all samples are consistent with fast growth rates, which are also verified by the growth rate measurements presented in Figure 10. Growth rates were calculated for K-feldspar formed in H_2O-saturated and H_2O-undersaturated conditions at 600 °C and 500 MPa. The growth rates in the Li-free samples (ΔT= 100 °C from the quartz-feldspar saturation curve and ΔT= 140 °C from the liquidus) range from $10^{-10.6}$ to $10^{-9.2}$ m/s. These measurements agree with the values measured by Swanson (1977) for alkali feldspar crystallized from synthetic granite with 3.5% H_2O at 800 MPa and 100 °C undercooling and by Baker and Freda (2001) for feldspars formed in the Orthoclase-Quartz-H_2O system at 50, 100 and 200 °C undercooling and 500 MPa. The Li-bearing samples (ΔT= 90-110 °C) exhibit one order of magnitude faster growth rates than the Li-

612 free runs, reaching $10^{-8.4}$ m/s for H_2O-saturated and $10^{-8.2}$ m/s for H_2O-undersaturated conditions,
613 respectively. Converting the highest growth rate values measured for the Li-free and Li-bearing
614 samples to cm per year renders values of about 2 and 13 cm/yr, respectively, for H_2O-saturated
615 experiments. We should note that these values represent minimum growth rates, assuming that
616 crystallization of the K-feldspar started immediately after the capsules reached 600 °C. Figure 10
617 also highlights the amount of crystallization achieved in the Li-free and the Li-bearing samples
618 by comparing the number of crystals. We note that in all measurements for both types of
619 experiments, only crystals with well-defined faces or edges in the backscattered images were
620 included. The number of crystals measured in the Li-free capsules represents almost 95% of the
621 total population of crystals generated, while in the Li-bearing samples about 60% of all
622 representative types of K-feldspar crystals developed were considered in the measurements. It
623 becomes apparent that the Li-free experiments created many fewer crystals in the same duration
624 of time than the Li-bearing runs. The bimodality of the distribution of growth rates in the Li-
625 bearing histograms reflects the formation of two groups of crystals, numerous tabular and small
626 skeletal crystals with slower growth rates and the few K-feldspar spherulites and larger skeletal
627 crystals that grew much faster.

628 ## DISCUSSION

629 ### The effect of Li on crystallization temperatures and the degree of undercooling

630 The positions of the liquidus and the solidus curves of the hydrous granitic system have
631 been studied by several researchers for various pressures and water contents (e.g., Tuttle and
632 Bowen 1958; Luth et al. 1964; Naney 1983; Johannes and Holtz 1996 and references therein).
633 Combining the data from the literature, we estimated that at 500 MPa the solidus of LCO lies at

634 approximately 645 °C. From our Li-free experiments we found that the liquidus lies at 740 °C
635 for the H_2O-saturated and at 780 °C for the H_2O-undersaturated granitic system. We should note
636 that experiments conducted with the unmodified LCO at 600 °C under H_2O-saturated conditions
637 did not reach the theoretical solidus of the system after 100 h, despite the presence of crystal
638 seeds as nuclei that facilitate crystallization. It seems that in the Li-free system the nucleation lag
639 time exceeded 100 h, the maximum duration of the experiments.

640 The experiments performed in this study show that the liquidus of the Li-enriched
641 hydrous granitic system lies at approximately 690-710 °C and the solidus at 450 °C at 500 MPa.
642 The addition of ~3700 ppm Li to the granitic system leads to an estimated decrease in the
643 liquidus temperature by about 50 °C for H_2O-saturated and 70 °C for H_2O-undersaturated
644 experiments, respectively, while the solidus temperature is lowered by 200 °C (Fig. 11). Our
645 results are consistent with those of Glyuk and Trufanova (1977) who evaluated the
646 crystallization and melting temperatures of the granite-H_2O system enriched with various
647 amounts of LiOH at 100 MPa. At this pressure the liquidus was estimated at 770-780 °C with the
648 addition of 3000 ppm Li and at 710-720 °C with 8000 ppm Li. The solidus dropped at 475 °C
649 when 5000 ppm Li were added to the system. A decrease in the solidus temperature was also
650 observed in other studies that investigated the effect of Li on the H_2O-saturated granitic system
651 at various pressures. Martin (1983) reported a 30 °C decrease with the addition of 9300 ppm Li
652 at 100 MPa, while at 275 MPa Wyllie and Tuttle (1964) evaluated a drop of the solidus
653 temperature by 90 °C with the addition of 11600 ppm Li. Vaughan (1964) estimated a decrease
654 in the crystallization and melting temperatures of the spodumene-bearing Harding pegmatite
655 (~3000 ppm Li) by 50 °C and 30 °C, respectively, at 500 MPa, compared with the liquidus and
656 solidus temperatures of the simple granitic Spruce Pine pegmatite in North Carolina (~45 ppm

Li). We emphasize that the experimental results of this study demonstrate that only 3700 ppm Li is enough to cause a significant decrease in the liquidus and solidus temperatures at 500 MPa. The decrease in the melting and crystallization temperatures is the result of depolymerization of the melt structure due to the presence of Li (Glyuk and Trufanova 1977; Martin 1983) and strongly suggests that Li acts as an effective fluxing agent in pegmatitic systems.

Most prevalent models for the genesis of pegmatites emphasize the important role of liquidus undercooling (London 2005; Simmons and Webber 2008). The formation of graphic and granophyric textures also appears highly dependent on the degree of undercooling, as shown in several experimental studies (Fenn 1986; Baker and Freda 2001; London 2005). Based on the experiments performed on Li-bearing samples in this study, pegmatitic textures, such as graphic and granophyric intergrowths between quartz and feldspar crystals (e.g., Fig. 3b-f and 5), start forming at about 85-90 °C undercooling in H_2O-undersaturated and H_2O-saturated runs. A comparison between the textures formed in the different Li-bearing experiments and the degree of undercooling shows that graphic and granophyric textures are generated at 85-110 °C undercooling, while in the Li-bearing samples that crystallized at higher values of undercooling the presence of graphic and granophyric intergrowths is highly restricted (Fig. 12). This degree of undercooling is lower than that reported for the formation of graphic textures on Li-free compositions in other experimental studies at 500 MPa (Fig. 13). Fenn (1986) relates the formation of graphic granite with undercooling between 145-165 °C, while Baker and Freda (2001) reproduce graphic intergrowths in experiments at 200 °C undercooling. On the other hand, Morgan and London (2012) report values between 50-150 °C for the generation of granophyre, which partially overlap with the 85-110 °C undercooling measured for graphic and granophyric textures in this study. From the above it becomes clear that the presence of Li in the

hydrous granitic system lowers substantially the degree of undercooling needed for the onset of the development of graphic and granophyric intergrowths to 85-90 °C, in comparison with the Li-free systems. Accordingly, pegmatite-forming melts that contain between 3% and 12% H_2O and less than 5000 ppm Li will start developing graphic and granophyric textures very early upon emplacement once crystallization commences at only moderately undercooled conditions.

Pegmatitic Textures

The experimental results of this study demonstrate that enrichment of the starting material with Li facilitates the development of the most characteristic features encountered in pegmatites (London 1992, 2008). The experiments that contained LCO, the Li-free starting material, only crystallized K-feldspar. In contrast, experiments with Li-LCO, containing ~3700 ppm Li, crystallized all three main pegmatitic minerals: K-feldspar, quartz and albite. Crystallization was greatly enhanced by the addition of Li to the system, as shown by the crystal fraction developed in experiments performed under the same conditions (500 MPa, 600 °C, 100 h), less than 2% for the Li-free and 12-80% for the Li-bearing samples, respectively. Variability of crystal sizes was also evident in the Li-bearing samples and lacking in the Li-free ones. In the former experiments, small skeletal or tabular K-feldspar crystals, from 1 to 50 μm maximum length, were formed in the vicinity of much larger K-feldspar spherulites, up to 1600 μm in diameter. In other parts of the capsules, fine-grained granophyric textures were developed among extensive K-feldspar crystals (500 μm in size), which were often accompanied by graphic quartz. Coarsening of the crystals from the center towards the edge of the crystallization front was observed in all Li-bearing samples. In addition, as crystallization progressed in the Li-bearing samples, Na-rich sectors formed on K-feldspar at the edge of the crystallization front. Experiments at 400 °C and 500 °C developed successive, almost monomineralic, K-feldspar,

703 albite and quartz zones, with a change in the shape of quartz crystals from anhedral to subhedral
704 at the edge of the crystallization front. Virgilite (or petalite, see discussion above) crystallized at
705 temperatures close to and below the solidus. More importantly, only the Li-bearing experiments
706 formed pegmatitic textures, with or without the presence of a separate aqueous phase. Graphic
707 and granophyric intergrowths between quartz and K-feldspar were reproduced in all capsules
708 with Li-LCO at 600 °C and 500 MPa, while none were formed in the Li-free experiments
709 conducted under the same conditions. The mechanisms involved in the generation of these
710 characteristic pegmatitic textures are discussed in the following paragraphs.

711 In his influential paper on the origin of graphic granite, Fenn (1986) proposed that
712 graphic intergrowths were disequilibrium textures developed in granitic systems through the
713 process of constitutional supercooling. Undercooling (or supercooling) is reported as the driving
714 force for the formation of granophyric intergrowths as well (Barker 1970; Morgan and London
715 2012). Fenn (1986) suggested that feldspar was formed first, with an initial planar interface
716 developing between the crystal and the melt. The planar interface was subsequently disrupted
717 due to local changes in the degree of undercooling, at which point a cellular interface was
718 formed, with parts of the feldspar growing faster than others and developing small projections
719 into the melt. The melt between these projections became locally saturated in components
720 excluded from the feldspar and enriched in the melt, such as excess SiO_2 and H_2O, and as a
721 result, quartz started crystallizing simultaneously with the feldspar.

722 The breakdown of a planar to a cellular interface and the faster growth of crystals due to
723 constitutional supercooling were first reported in experiments on metals by Tiller and Rutter
724 (1956). They noted that very small quantities of solute were enough to cause constitutional
725 supercooling and form the perturbations on the crystal/melt interface. Lentz and Fowler (1992)

agreed that the fast growth of the feldspar due to undercooling leads to the development of rough surfaces on the faces of the crystals on which quartz then nucleated and grew epitaxially. Although both Fenn (1970) and Tiller and Rutter (1956) agree that a combination of the morphology of the crystal/melt interface and constitutional supercooling lead to the fast growth of crystals, they do not explain the mechanism that causes the initial breakdown of the interface from planar to cellular.

We suggest that a change in the morphology of the interface between the K-feldspar and the melt from planar to cellular takes place in the Li-bearing experiments and that this change is related to undercooling and the different ionic radius of Li^+ in comparison with K^+ and Na^+. Deubener et al. (1991) conducted a series of ion exchange experiments on feldspars and evaluated the effect of different cations occupying the M site of the crystals. They observed a decrease of 8%, 2.5% and 2% in the a, b and c lattice constants, respectively, for $LiAlSi_3O_8$ crystals in comparison with the original Li-free sanidine, orthoclase and adularia crystals used in the experiments. They also showed that M site substitution in the MO_x polyhedron results in a difference in coordination number for the prevalent cations (X for K^+, VIII for Na^+ and V for Li^+). As a result, the presence of Li^+ ions in the M site places considerable strain on the feldspar framework and the amount of Li that can be accommodated in the structure of the feldspar is expected to be restricted. This observation is verified by the experiments in this study since K-feldspar crystals developed in Li-bearing samples incorporate a maximum of 250 ppm Li with the remainder Li concentrating in the residual melt. Additionally, since the feldspar framework can be modified by the presence of Li^+ ions (Deubener at al. 1991), we propose that the substitution of Li^+ for K^+ and Na^+ ions in the crystal structure of the feldspar leads to breakdown of planar growth and a shift to cellular growth. The development of an irregular surface could be

749 the reflection of the strain placed on the feldspar structure where Li substitution is established
750 and feldspar crystals consist of a combination of MO_x polyhedra with different monovalent
751 cations. The faster growth rates measured for K-feldspar crystals in the Li-bearing samples
752 compared with the Li-free experiments (see previous section on growth rates) further support the
753 incorporation of Li^+ ions in the structure of the feldspar and the resulting shift from a planar to a
754 cellular feldspar/melt interface.

755 Evidence of the development of a cellular K-feldspar/melt interface can be seen in Figure
756 14 which portrays images of Li-bearing experiments with 6% H_2O, performed at 625 °C, 500
757 MPa. At 625 °C the experiment is close to the liquidus of the system (ΔT= 85 °C) and individual
758 K-feldspar crystals with skeletal or tabular morphology appear to be forming before quartz.
759 Perturbations started to develop on the growing feldspar crystal resulting in some parts of the
760 faces growing faster than others. In the small areas between the faster growing projections of the
761 feldspar the melt was depleted in K and Al, the essential structural elements of K-feldspar, and
762 the activity of SiO_2 increased resulting in the crystallization of quartz. Close inspection of the
763 interface between K-feldspar crystals and quartz shows a slightly rough irregular surface, often
764 with trapped vesicles that represent H_2O excluded from the feldspars (Fig. 14a, c). Quartz started
765 growing on that irregular surface, in the areas between the small fast-growing projections of the
766 feldspar, initially forming a thin discontinuous layer and subsequently alternating with K-
767 feldspar when enough K and Al concentrated again in the melt close to the crystallization front.
768 Repetition of this process seems to result in granophyric quartz-feldspar intergrowths.
769 Alternating crystallization of feldspar and quartz on a cellular interface, combined with fast
770 growth rates and sufficient undercooling (Fenn 1986) can explain the formation of the pegmatitic

771 textures in the Li-bearing experiments, in contrast with the Li-free runs where no intergrowths
772 were developed at even greater degrees of undercooling (ΔT= 100-140 °C).

773 The same mechanism responsible for the generation of the granophyric intergrowths in
774 the experimental samples is almost certainly operating in the case of the graphic textures as well.
775 However, the differences in the morphology and size of the crystals between the two textures
776 indicate that some properties of the melt at the interface with the growing crystals change in the
777 transition from one to the other. The presence of 5% Li_2O in a melt of haplogranitic composition
778 is known to decrease the viscosity by approximately two orders of magnitude at temperatures
779 close to 600 °C and 1 atm (Hess et al. 1995). Bartels et al. (2011) also suggest that hydrous
780 pegmatitic melts with a low aluminum saturation index have even lower viscosity than
781 compositionally similar melts with fewer fluxing components. We showed earlier that the
782 addition of ~3700 ppm Li in the starting material used in this study shifted the composition of
783 the melt from peraluminous to peralkaline. Consequently, we expect that changes in the Li
784 content of the melt in the experimental samples could lead to local changes in the viscosity of the
785 melt in front of the growing quartz and feldspar crystals, which could explain the transition from
786 granophyric to graphic textures. The fast growing feldspar crystals incorporate approximately
787 one order of magnitude more Li than quartz formed in the same experiments (Table 3).
788 Therefore, the melt in front of the growing feldspar should contain less Li, K and Na in
789 comparison to the melt in front of the quartz since those elements are incorporated at higher
790 concentrations into the feldspar than the quartz. As a result, the viscosity of the melt in front of
791 the feldspar should be slightly increased locally compared to the melt in front of the quartz,
792 which could have an effect on the growth rate of the crystals.

In order to test this hypothesis, we compared the growth rate of quartz from the granophyric and the graphic textures shown in Figure 14 and the results are presented in Figure 15. To calculate the growth rate in both textures, we measured the longest dimension of the quartz crystals and divided by the duration of the experiment. The growth rates of graphic quartz are close to one order of magnitude faster than those of the quartz from the granophyric intergrowths. As the granophyric quartz-feldspar intergrowth is developed, the feldspar seems to be gradually slowing down forming a much more regular surface at the contact with the melt (Fig. 14b-d) compared with the initial irregular interface. At the same time, quartz is gradually growing faster in a melt richer in fluxing components and develops crystals with larger size and cuneiform morphology (Fig. 14d). How strong the effect of one order of magnitude difference in Li content (181 ppm Li in K-feldspar compared to 7 ppm Li in quartz) will be on the expected decrease in viscosity in front of the growing crystals is not known. However, it was shown in previous studies that the decrease in viscosity with the addition of Li is more pronounced in the first few wt. % of added Li_2O and becomes increasingly smaller at more elevated concentrations (Hess et al. 1995; Dingwell et al. 1996). So, possibly a difference of one order of magnitude in Li content of the melt in front of the growing crystals is enough to cause the observed textural changes in the quartz-feldspar intergrowths. We attempted to measure the Li concentration of the melt in front of the growing K-feldspar and quartz crystals using a very small step and beam diameter. Unfortunately, the smallest beam diameter we were able to obtain with SIMS for Li analysis was 15 μm which was unable to detect any difference in Li concentrations at the crystal/melt interface. We also tried to examine the effect of Li at the crystal/melt interface indirectly by analyzing Al by electron microprobe, since Al is the charge-balancing cation for Li in quartz and Li-bearing feldspar. Analyses with EMPA along traverses at the crystal/melt

interface with a 3 μm step and a 3 μm beam diameter did not reveal significant differences in Al content of the melt which possibly implies that any variations in Li content of the melt in front of the quartz and feldspar crystals are generated less than 3 μm away from the crystal/melt interface.

The experimental results from this study at 500 MPa pressure and 400-800 °C temperature demonstrate that Li is an effective fluxing component of the pegmatite-forming melt. The presence of ~3700 ppm Li in the hydrous granitic system is enough to lower the crystallization and melting temperatures by 50-70 °C and 200 °C, respectively, enhance crystallization, increase the growth rate of K-feldspar by one order of magnitude and reduce the degree of undercooling required for the onset of formation of pegmatitic textures to only 85-90 °C. The amount of H_2O does not seem to greatly affect the textures developed in the Li-enriched granitic system since graphic and granophyric intergrowths were formed in both H_2O-saturated and H_2O-undersaturated conditions. Li-aluminosilicates were formed in experiments at lower temperatures during the last stages of crystallization, confirming that Li behaves incompatibly in relation to other minerals and accumulates preferentially in the residual melt. The coarse-grained appearance of the crystals in the capsules, the variability of crystal sizes, the presence of heterogeneous graphic and granophyric intergrowths between quartz and K-feldspar and the crystallization of Li-aluminosilicates are all typical features encountered in natural Li-bearing pegmatites that were reproduced in the Li-enriched experiments.

IMPLICATIONS

Fluxing agents have long been recognized as an indispensable component of pegmatite-forming melts and their role is incorporated in the prevalent models on the genesis of pegmatites.

838 This study demonstrates that graphic and granophyric intergrowths between quartz and feldspar
839 are generated at lower degrees of undercooling in Li-bearing hydrous granitic melts compared
840 with Li-free melts of the same composition. Consequently, quartz and feldspar crystals can start
841 forming earlier upon emplacement of a pegmatite-forming melt than previously thought. The
842 small amount of Li (~3700 ppm) necessary to produce granophyric and graphic textures at
843 relatively low degrees of undercooling relaxes the constraint that granitic magmas must be
844 undercooled by several hundreds of degrees to form pegmatites. Furthermore, feldspar crystals
845 developed in the Li-bearing system can incorporate 150-250 ppm Li and grow at a rate of 13
846 cm/yr, one order of magnitude faster than feldspar in the Li-free system. The remaining Li
847 preferentially partitions in the melt, leading to the generation of a highly evolved residual melt.
848 Monomineralic zones are developed at lower temperatures as crystallization progresses, with Li-
849 aluminosilicates being the last product of crystallization of this Li-enriched evolved melt. The
850 demonstrated effects of only small amounts of Li on the textural evolution of our experiments
851 suggests that this element may also play a significant role in small, pegmatitic patches
852 occasionally found in granitic plutons. The results of this study confirm that the crystallization
853 interval of Li-bearing pegmatites is very narrow, approximately 250 °C, and crystallization is
854 very rapid. This observation, in combination with the fact that Li-bearing pegmatites are usually
855 found at long distances from the parent granites, strengthens the hypothesis that these highly
856 evolved melts are very mobile and they contain a significant amount of accumulated fluxing
857 components, among the most effective of which is Li. Finally, our study suggests that with
858 further research the crystallization behavior of Li-bearing ceramics may be better understood and
859 tailored to produce materials whose properties are more finely-tuned by a combination of
860 varying the Li concentration and the degree of undercooling.

ACKNOWLEDGEMENTS

The authors wish to thank E. Bruce Watson for kindly providing the LCO starting material and Jeanne Paquette for supplying the K-feldspar crystals used in the experiments. We would also like to express our appreciation to David London, Gary Lofgren and Alexander Bartels for their official reviews which greatly benefited the original manuscript. The present study was supported by an NSERC Discovery Grant to D.R.B.

REFERENCES CITED

Baker, D.R. (1991) Interdiffusion of hydrous dacitic and rhyolitic melts and the efficacy of rhyolite contamination by dacitic enclaves. Contributions to Mineralogy and Petrology, 106, 462-473.

Baker, D.R. (2004) Piston-cylinder calibration at 400 to 500 MPa: A comparison of using water solubility in albite melt and NaCl melting. American Mineralogist, 89, 1553-1556.

Baker, D.R., and Alletti, M. (2012) Fluid saturation and volatile partitioning between melts and hydrous fluids in crustal magmatic systems: The contribution of experimental measurements and solubility models. Earth-Science Reviews, 114, 298-324.

Baker, D.R., and Freda, C. (2001) Eutectic crystallization in the undercooled orthoclase-quartz-H_2O system: experiments and simulations. European Journal of Mineralogy, 13, 453-466.

Baker, D.R., Conte, A.M., Freda, C., and Ottolini, L. (2002) The effect of halogens on Zr diffusion and zircon dissolution in hydrous metaluminous granitic melts. Contributions to Mineralogy and Petrology, 142, 666-678.

881 Barker, D.S. (1970) Compositions of granophyre, myrmekite, and graphic granite. Geological
882 Society of America Bulletin, 81, 3339-3350.

883 Bartels, A., Vetere, F., Holtz, F., Behrens, H., and Linnen, R.L. (2011) Viscosity of flux-rich
884 pegmatitic melts. Contributions to Mineralogy and Petrology, 162, 51-60.

885 Behrens, H., Meyer, M., Holtz, F., Benne, D., and Nowak, M. (2001) The effect of alkali ionic
886 radius, temperature and pressure on the solubility of water in $MAlSi_3O_8$ melts (M=Li, Na,
887 K, Rb). Chemical Geology, 174, 275-289.

888 Burnham, C.W. (1979) The importance of volatile constituents. In H.S. Yoder, Ed., The evolution
889 of the igneous rocks, p. 439-482. Princeton University Press, Princeton, NJ.

890 Cerny, P. (1991) Rare-element granite pegmatites I. Anatomy and internal evolution of
891 pegmatite deposits. Geoscience Canada, 18, 527-543.

892 Cross, W., Iddings, J.P., Pirsson, L.V., and Washington, H.S. (1902) A quantitative chemico-
893 mineralogical classification and nomenclature of igneous rocks. Journal of Geology, 10,
894 555-610.

895 Dingwell, D.B., Romano, C., and Hess, K.U. (1996) The effect of water on the viscosity of a
896 haplogranitic melt under P-T-X conditions relevant to silicic volcanism. Contributions to
897 Mineralogy and Petrology, 124, 19-28.

898 Dingwell, D.B., Holtz, F., and Behrens, H. (1997) The solubility of H_2O in peralkaline and
899 peraluminous granitic melts. American Mineralogist, 82, 434-437.

900 Deubener, J., Sternitzke, M., and Müller, G. (1991) Feldspars $MAlSi_3O_8$ (M=H, Li, Ag)
901 synthesized by low-temperature ion exchange. American Mineralogist, 76, 1620-1627.

Evensen, J.M. (2001) The geochemical budget of beryllium in silicic melts and superliquidus, subliquidus, and starting state effects on the kinetics of crystallization in hydrous haplogranite melts. Unpbl. PhD thesis, University of Oklahoma, p. 293.

Fenn, P.M. (1977) The nucleation and growth of alkali feldspars from hydrous melts. Canadian Mineralogist, 15, 135-161.

Fenn, P.M. (1986) On the origin of graphic granite. American Mineralogist, 71, 325-330.

Glyuk D.S, and Trufanova L.G. (1977) Melting at 1000 kg/cm^2 in a granite-H_2O system with the addition of HF, HCL, and Li, Na, and K fluorides, chlorides, and hydroxides. Geochemistry International, 14, 28-36.

Grosjean, C., Miranda, P.H., Perrin, M., and Poggi, P. (2012) Assessment of world lithium resources and consequences of their geographic distribution on the expected development of the electric vehicle industry. Renewable and Sustainable Energy Reviews, 16, 1735-1744.

Gualda, G.A.R., Ghiorso M.S., Lemons R.V., and Carley T.L. (2012) Rhyolite-MELTS: a modified calibration of MELTS optimized for silica-rich, fluid-bearing magmatic systems. Journal of Petrology, 53, 875-890.

Harrison, T.M., and Watson, E.B. (1983) Kinetics of zircon dissolution and zirconium diffusion in granitic melts of variable water content. Contributions to Mineralogy and Petrology, 84, 66-72.

Hess, K.U., Dingwell, D.B., and Webb, S.L. (1995) The influence of excess alkalis on the viscosity of a haplogranitic melt. American Mineralogist, 80, 297-304.

Holloway, J.R., and Wood, B.J. (1988) Simulating the earth: experimental geochemistry, p. 196, Unwin Hyman Ltd, London.

Hudon, P., Baker, D.R., and Toft, P.B. (1994) A high-temperature assembly for 1.91-cm (3/4-in.) piston cylinder apparatus. American Mineralogist, 79, 145-147.

Jahns, R.H. (1953) The genesis of pegmatites II. Quantitative analysis of lithium-bearing pegmatite, Mora County, New Mexico. American Mineralogist, 38, 1078-112.

Jahns, R.H., and Burnham, C.W. (1969) Experimental studies of pegmatite genesis. I. A model for the derivation and crystallization of granitic pegmatites. Economic Geology, 64, 843-864.

Jaskula, B.W. (2012) Lithium. Mineral Commodities Summaries, US Geological Survey.

Johannes, W., and Holtz, F. (1996) Petrogenesis and experimental petrology of granite rocks. In Minerals and Rocks 22, p. 335. Springer-Verlang, Berlin.

Lachowski, E.E., Murray, L.W., and Taylor, H.F.W. (1979) Truscottite: composition and ionic substitutions. Mineralogical Magazine, 43, 333-336.

Lentz, D.R., and Fowler, A.D. (1992) A dynamic model for graphic quartz-feldspar intergrowths in granitic pegmatites in the southwestern Grenville Province. American Mineralogist, 30, 571-585.

Linnen R.L., Van Lichtervelde, M., and Cerny, P. (2012) Granitic pegmatites as sources of strategic metals. Elements, 8, 275-280.

London, D. (1992) The application of experimental petrology to the genesis and crystallization of granitic pegmatites. Canadian Mineralogist, 30, 499-540.

London, D. (2005) Granitic pegmatites: an assessment of current concepts and directions for the future. Lithos, 80, 281-303.

London, D. (2008) Pegmatites, 347 p. Canadian Mineralogist, Special Publication 10, Mineralogical Association of Canada.

London, D., and Burt, D.M. (1982) Lithium aluminosilicate occurrences in pegmatites and the lithium aluminosilicate phase diagram. American Mineralogist, 67, 483-493.

London, D., Morgan, G.B. VI, and Hervig, R.L. (1989) Vapor-undersaturated experiments in the system macusanite-H_2O at 200MPa, and the internal differentiation of granitic pegmatites. Contributions to Mineralogy and Petrology, 102, 1-17.

Luth, W.C., Jahns, R.H., and Tuttle, O.F. (1964) The granite system at pressures of 4 to 10 kilobars. Journal of Geophysical Research, 69, 759-773.

Macfarlane, A.W., and Shimizu, N. (1991) SIMS measurements of $\delta^{34}S$ in sulphide minerals from adjacent vein and stratabound ores. Geochimica et Cosmochimica Acta, 55, 525-541.

Maloney, J.S., Nabelek, P.I., Sirbescu, M.L.C., and Halama, R. (2008) Lithium and its isotopes in tourmaline as indicators of the crystallization process in the San Diego County pegmatites, California, USA. European Journal of Mineralogy, 20, 905-916.

Manning, D.A.C. (1981) The effect of fluorine on liquidus phase relationships in the system Qz-Ab-Or with excess water at 1 kb. Contributions to Mineralogy and Petrology, 76, 206-215.

962 Martin, J.S. (1983) An experimental study of the effects of lithium on the granite system.
963 Proceedings of the Ussher Society, 5, 417-420.

964 Morgan, G.B. VI, and London, D. (1996) Optimizing the electron microprobe analysis of
965 hydrous alkali aluminosilicate glasses. American Mineralogist, 81, 1176-1185.

966 Morgan, G.B. VI, and London, D. (2012) Process of granophyre crystallization in the Long
967 Mountain Granite, southern Oklahoma. Geological Society of America Bulletin, 124,
968 1251-1261.

969 Naney, M.T. (1983) Phase equilibria of rock-forming ferromagnesian silicates in granitic
970 systems. American Journal of Science, 283, 993-1033.

971 Papale P. (1997) Thermodynamic modeling of the solubility of a one-component H_2O or CO_2
972 fluid in silicate liquids. Contributions to Mineralogy and Petrology, 126, 237-251.

973 Partington, G.A., McNaughton, N.J., and Williams, I.S. (1995) A review of the geology,
974 mineralization and geochronology of the Greenbushes pegmatite, Western Australia.
975 Economic Geology, 90, 616-635.

976 Potter, E.G., Taylor, R.P., Jones, P.C., Lalonde, A.E., Pearse, G.H.K., and Rowe, R. (2009)
977 Sokolovaite and evolved lithian micas from the eastern Moblan granitic pegmatite, Opatica
978 subprovince, Quebec, Canada. Canadian Mineralogist, 47, 337-349.

979 Richter, F.M., Davis, M.A., DePaolo, D.J., and Watson, E.B. (2003) Isotope fractionation by
980 chemical diffusion between molten basalt and rhyolite. Geochimica et Cosmochimica
981 Acta, 67, 3905-3923.

Roda, E., Pesquera, A., and Velasco, F. (1995) Micas of the muscovite-lepidolite series from the Fregeneda pegmatites (Salamanca, Spain). Mineralogy and Petrology 55, 145-157.

Romano, C., Dingwell, D.B., Behrens, H., and Dolfi, D. (1996) Compositional dependence of H_2O solubility along the joins $NaAlSi_3O_8$-$KAlSi_3O_8$, $NaAlSi_3O_8$-$LiAlSi_3O_8$, and $KAlSi_3O_8$-$LiAlSi_3O_8$. American Mineralogist, 81, 452-461.

Romano, C., Poe, B., Mincione, V., Hess, K.U., and Dingwell, D. (2001) The viscosities of dry and hydrous $XAlSi_3O_8$ (X=Li, Na, K, $Ca_{0.5}$, $Mg_{0.5}$) melts. Chemical Geology, 174, 115-132.

Simmons, W.B., and Webber, K.L. (2008) Pegmatite genesis: state of the art. European Journal of Mineralogy, 20, 421-438.

Sirbescu M.L.C, and Nabelek P.I. (2003) Crustal melts below 400 °C. Geology, 31, 685-688.

Swanson, S.E. (1977) Relation of nucleation and crystal-growth rate to the development of granitic textures. American Mineralogist, 62, 966-978.

Thomas, R., Davidson, P., and Beurlen, H. (2012) The competing models for the origin and internal evolution of granitic pegmatites in the light of melt and fluid inclusion research. Mineralogy and Petrology, 106, 55-73.

Tiller, W.A., and Rutter, J.W. (1956) The effect of growth conditions upon the solidification of a binary alloy. Canadian Journal of Geophysics, 34, 96-121.

Tuttle, O.F., and Bowen, N.L. (1958) Origin of granite in the light of experimental studies in the system $NaAlSi_3O_8$-$KAlSi_3O_8$-SiO_2-H_2O. In Memoirs, 74, p. 153. Geological Society of America.

1003 Vaughan, D. E. W. (1964). The crystallization ranges of the Spruce Pine and Harding
1004 pegmatites. Unpbl. MSc thesis, Pennsylvania State University, p. 61.

1005 Webber, K.L., Simmons, W.B., Falster, A.U., and Foord, E.E. (1999) Cooling rates and
1006 crystallization dynamics of shallow level pegmatite-aplite dikes, San Diego County,
1007 California. American Mineralogist, 84, 708-717.

1008 Wyllie, P.J., and Tuttle, O.F. (1964) Experimental investigation of silicate systems containing
1009 two volatile components. Part III. The effects of SO_3, P_2O_5, HCl and Li_2O, in addition to
1010 H_2O, on the melting temperature of albite and granite. American Journal of Science, 262,
1011 930-939.

1012 **FIGURE CAPTIONS**

1013 **Figure 1.** Schematic of the experimental capsules that contain crystal seeds. LCO: Lake
1014 County obsidian (starting material).

1015 **Figure 2.** Backscattered images of Li-free samples with 12% H_2O at 600 °C ($\Delta T \sim$ 100-
1016 140 °C, 500 MPa, 100 h). a) PGT 28: Skeletal K-feldspar crystals developed in melt with
1017 vesicles, 2% crystallization. The white rim surrounding the glass is the wall of the capsules. b)
1018 PGT 28: Skeletal and tabular K-feldspar crystals developed in melt together with a bladed Ca-
1019 silicate phase. Kfs: K-feldspar, Ca-sil: Ca-silicate mineral (see text for discussion), gls: glass, V:
1020 vesicles.

1021 **Figure 3.** Backscattered images of Li-bearing samples with 6-12% H_2O at 625 °C ($\Delta T \sim$
1022 85 °C, 500 MPa, 100 h). a) PGT 57: Subhedral clinopyroxene crystal and the bladed Ca-silicate
1023 phase in glass with vesicles (12% H_2O). b-f) PGT 58: K-feldspar and quartz forming graphic and

1024 granophyric intergrowths (6% H_2O). Skeletal K-feldspar crystals seem to be forming first
1025 followed by granophyric and graphic textures (see text and Figure 14). The white rim on the top
1026 left is the wall of the capsules. Kfs: K-feldspar, Qz: quartz, Cpx: clinopyroxene, Ca-sil: Ca-
1027 silicate mineral, GT: graphic texture, GRN: granophyric texture, gls: glass, V: vesicles.

1028 **Figure 4.** Qz-Ab-Or ternary plot with average CIPW normative wt. % values calculated
1029 from EMPA analytical traverses (10-80 analyses performed per traverse) on graphic and
1030 granophyric textures in Li-bearing samples (500 MPa, 100 h). Solid symbols represent graphic
1031 textures and empty symbols granophyric textures. Triangles facing up: 12% H_2O and 600 °C,
1032 triangles facing down: 6% H_2O and 600 °C, circles: 6% H_2O and 625 °C, squares: average
1033 values for granophyric and graphic textures from Barker (1970), star: granite minimum
1034 composition at 500 MPa (from Luth et al. 1964).

1035 **Figure 5.** Backscattered images of Li-bearing samples with 12% H_2O at 600 °C ($\Delta T \sim 90$
1036 °C, 500 MPa, 100 h). a-c) PGT 15-16: Skeletal K-feldspar crystals developed in melt with
1037 vesicles, 13% crystallization. Graphic and granophyric intergrowths formed between K-feldspar
1038 and quartz. d) PGT 34: Graphic and granophyric textures between K-feldspar and quartz formed
1039 in melt, 29% crystallization. Notice the coarsening of the feldspars and the development of albite
1040 at the edge of the crystallization front. The white rim on the top right is the wall of the capsules.
1041 Kfs: K-feldspar, Qz: quartz, Ab: albite, GT: graphic texture, GRN: granophyric texture, gls:
1042 glass, V: vesicles.

1043 **Figure 6.** Backscattered images of Li-bearing samples with 6% H_2O at 600 °C ($\Delta T \sim 110$
1044 °C, 500 MPa, 100 h). a) PGT 17: K-feldspar spherulites growing in melt and surrounded by
1045 vesicles, 65% crystallization. The white rim surrounding the spherulites is the wall of the

capsules. b) PGT 17: Granophyric quartz-feldspar textures and coarser K-feldspar crystals at the edge of the spherulites surrounded by glass and vesicles. Notice the formation of Na-rich sectors (Ab). c) PGT 19: Graphic and granophyric textures between quartz and K-feldspar with skeletal and spherulitic morphologies formed in melt with vesicles, 40% crystallization. Notice the development of albite at the edge of the crystallization front. d) PGT 17: Alternating graphic and granophyric textures in parallel arrangement generated in melt with coarser K-feldspar crystals forming at the edge of the crystallization front. Kfs: K-feldspar, Qz: quartz, Ab: albite, Cpx: clinopyroxene, GT: graphic texture, GRN: granophyric texture, gls: glass, V: vesicles.

Figure 7. Backscattered images of Li-bearing samples with 3% H_2O at 600 °C ($\Delta T \sim 110$ °C, 500 MPa, 100 h). a) PGT 30: K-feldspar spherulites growing in melt and surrounded by vesicles, 81% crystallization. The white rim surrounding the spherulites is the wall of the capsule. b) PGT 31: K-feldspar spherulites with coarser tabular crystals at the edge of the crystallization front surrounded by glass and vesicles, 54% crystallization. c) PGT 30: Coarser tabular K-feldspar crystals forming at the edge of the spherulites with sectors rich in albite. d) PGT 31: K-feldspar crystals with spherulitic morphology developing together with graphic and granophyric intergrowths. Kfs: K-feldspar, Qz: quartz, Ab: albite, Ca-sil: Ca-silicate mineral, GT: graphic texture, GRN: granophyric texture, gls: glass, V: vesicles.

Figure 8. Backscattered images of Li-bearing samples with 12% H_2O at 500 °C ($\Delta T \sim$ 190 °C, 500 MPa, 100 h). a) PGT 59: K-feldspar zone followed by albite growing in melt and vesicles, 12% residual melt. Notice the development of large cavities by the aqueous phase (V). The white rim surrounding the crystals is the wall of the capsule. b) PGT 59: Detail of the melt pool with K-feldspar, albite and subhedral virgilite crystals forming at the edge of the crystallization front. c) PGT 59: K-feldspar, albite and quartz in successive, almost

monomineralic zones. Quartz forms coarse subhedral crystals close to the aqueous phase. d) PGT 59: K-feldspar and quartz in graphic intergrowths. Sectors rich in albite can also be seen close to the graphic textures. Kfs: K-feldspar, Qz: quartz, Ab: albite, Vgl: virgilite, GT: graphic texture, gls: glass, V: vesicles.

Figure 9. Backscattered images of Li-bearing samples with 12% H_2O at 400 °C ($\Delta T \sim$ 290 °C, 500 MPa, 100 h). a) PGT 52: Clusters comprised of K-feldspar, albite and quartz zones. Virgilite appears to be the last phase that crystallizes. Notice the development of large cavities by the aqueous phase (V). The white rim surrounding the clusters is the wall of the capsule. b) PGT 52: Detail of the previous image with K-feldspar and albite zones, followed by subhedral quartz. c) PGT 51: K-feldspar, albite and quartz in successive, almost monomineralic zones. Quartz forms coarse subhedral crystals at the crystallization front close to the aqueous phase. d) PGT 52: Anhedral virgilite crystals as the last product of crystallization following quartz. Kfs: K-feldspar, Qz: quartz, Ab: albite, Vgl: virgilite, GT: graphic texture, gls: glass, V: vesicles.

Figure 10. Growth rates calculated for K-feldspar crystals formed in Li-free and Li-bearing experiments with 3-12% H_2O (500 MPa, 600 °C, 100 h). Notice the small number of crystals in the Li-free samples in comparison with the Li-bearing runs. Growth rates measured for the Li-bearing feldspars are one order of magnitude faster than the Li-free samples.

Figure 11. Temperature versus wt. % H_2O phase diagram of the hydrous granitic system at 500 MPa pressure based on results of this study and in the literature. Dashed lines: liquidus and solidus curves of the Li-free hydrous granitic system (solidus based on data from Tuttle and Bowen 1958, Luth et al. 1964, Naney 1983). The Qz-Afs saturation curve is also shown. Solid lines: liquidus and solidus curves of the hydrous granitic system enriched with 3700 ppm Li. The

Qz-Afs saturation curve coincides with the liquidus. Cpx: clinopyroxene, Pl: plagioclase, Afs: alkali feldspar, Kfs: K-feldspar, Ab: albite, Qz: quartz, Ca-sil: Ca-silicate, Vgl: Virgilite, L: liquid, V: aqueous phase.

Figure 12. Diagram relating the degree of undercooling (ΔT) with the prevalent K-feldspar crystal morphologies and pegmatitic textures developed in Li-bearing experiments at 500 MPa. Sk: skeletal crystals, Sph: spherulitic crystals, GRN: granophyric textures, GT: graphic textures, MZ: monomineralic zones.

Figure 13. The effect of Li on the degree of undercooling (ΔT) leading to the formation of graphic and granophyric textures. Undercooling values obtained in previous Li-free experiments (Fenn 1986; Baker and Freda 2001; Morgan and London 2012) are higher than the values obtained in this study.

Figure 14. Backscattered images of the same Li-bearing sample from Figure 3b-f. Skeletal K-feldspar crystals exhibit irregular surfaces (in circle in a and c) where quartz is developing. Simultaneous crystallization of feldspar and quartz forms the granophyric intergrowths that surround the crystals. The granophyric textures coarsen toward the direction of growth (white arrows in b and c) generating graphic textures between K-feldspar and quartz crystals, which gradually grow in parallel arrangement (b-d). Kfs: K-feldspar, Qz: quartz, GT: graphic texture, GRN: granophyric texture, gls: glass.

Figure 15. Growth rates calculated for quartz crystals in granophyric and graphic intergrowths with the K-feldspar seen in Figure 14c (Li-bearing experiments with 6% H_2O, 500 MPa, 625 °C, 100 h). The growth rate of the host K-feldspar is estimated at 10^{-10} m/s.

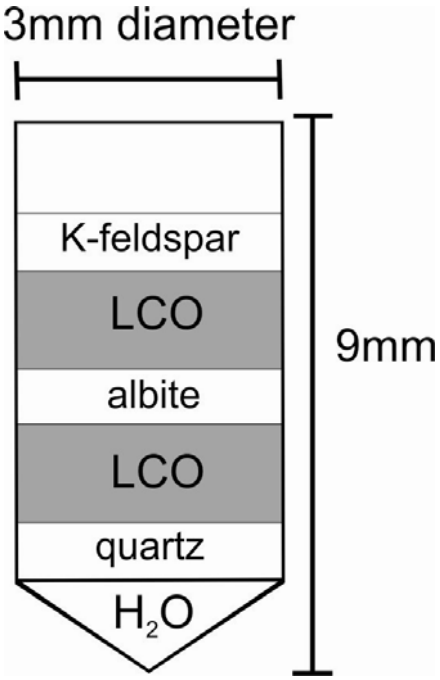

1112

1113 Figure 1

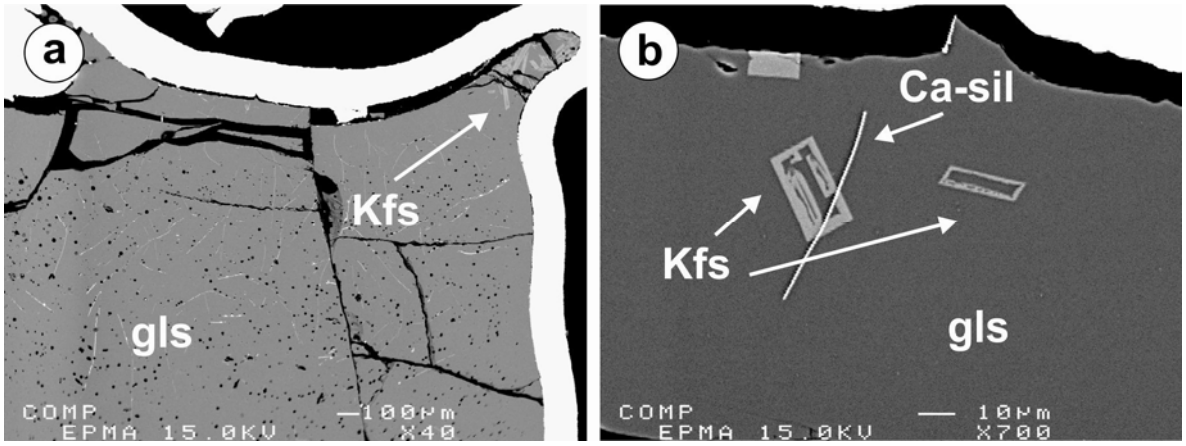

1114

1115 Figure 2

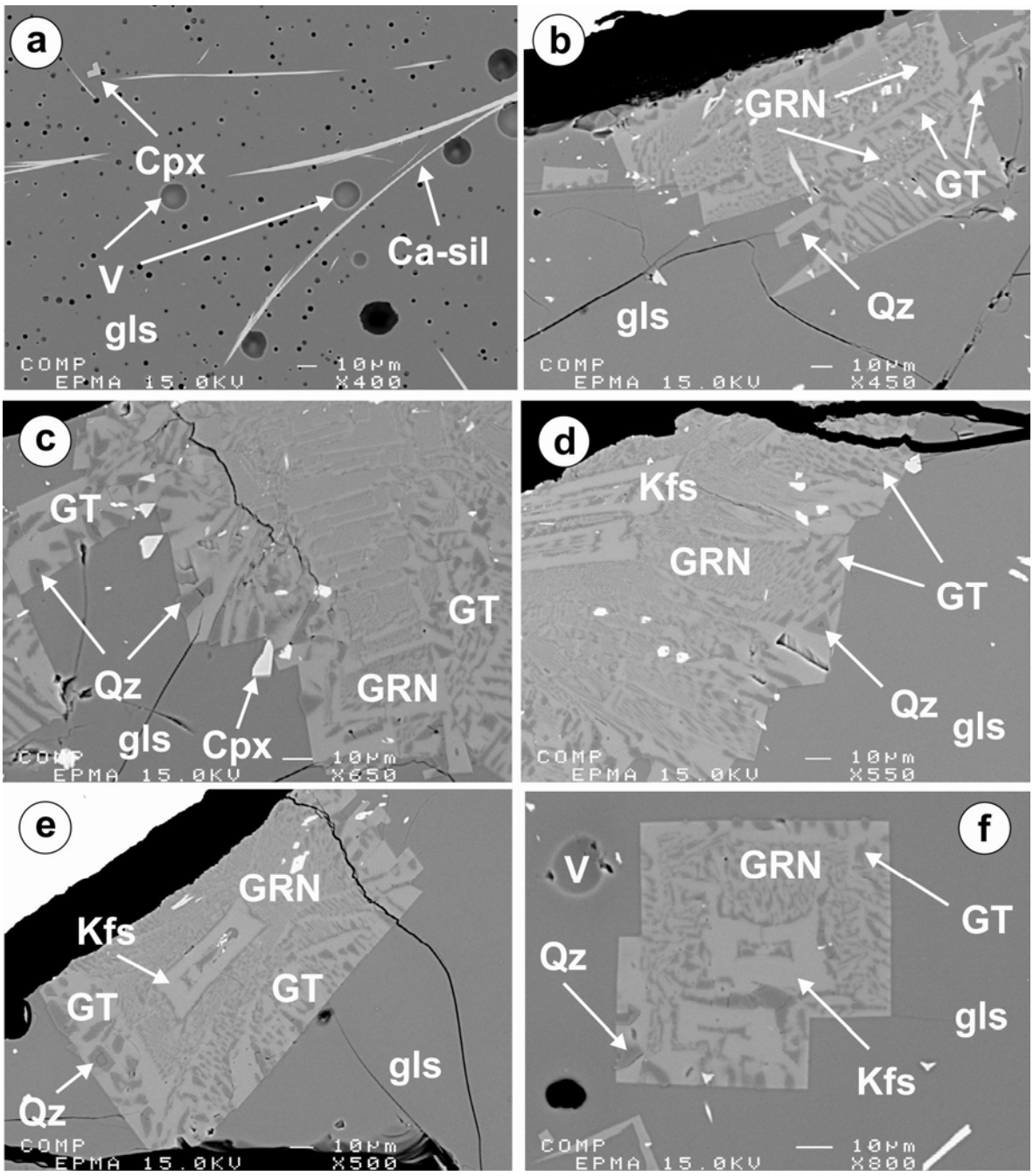

Figure 3

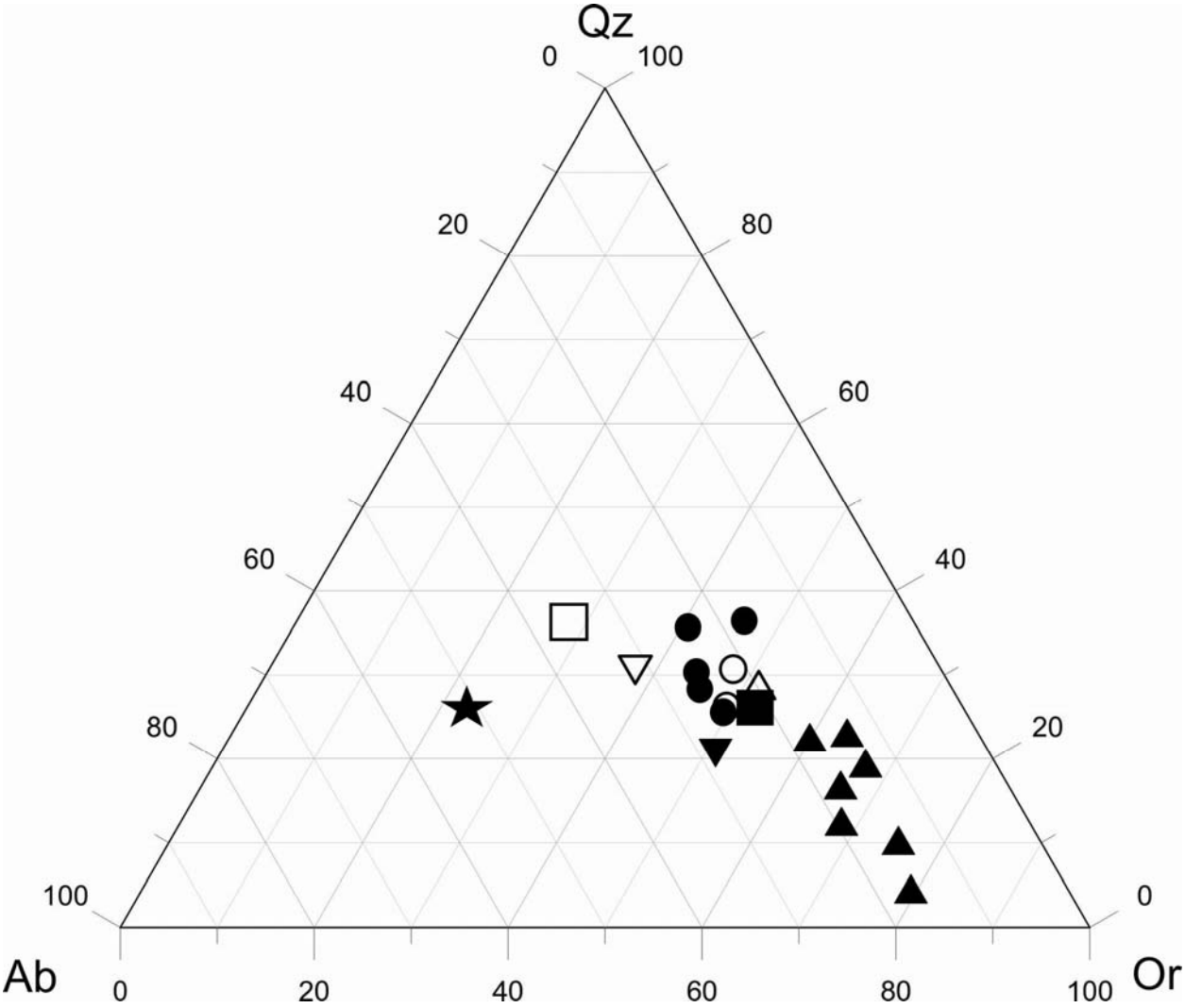

Figure 4

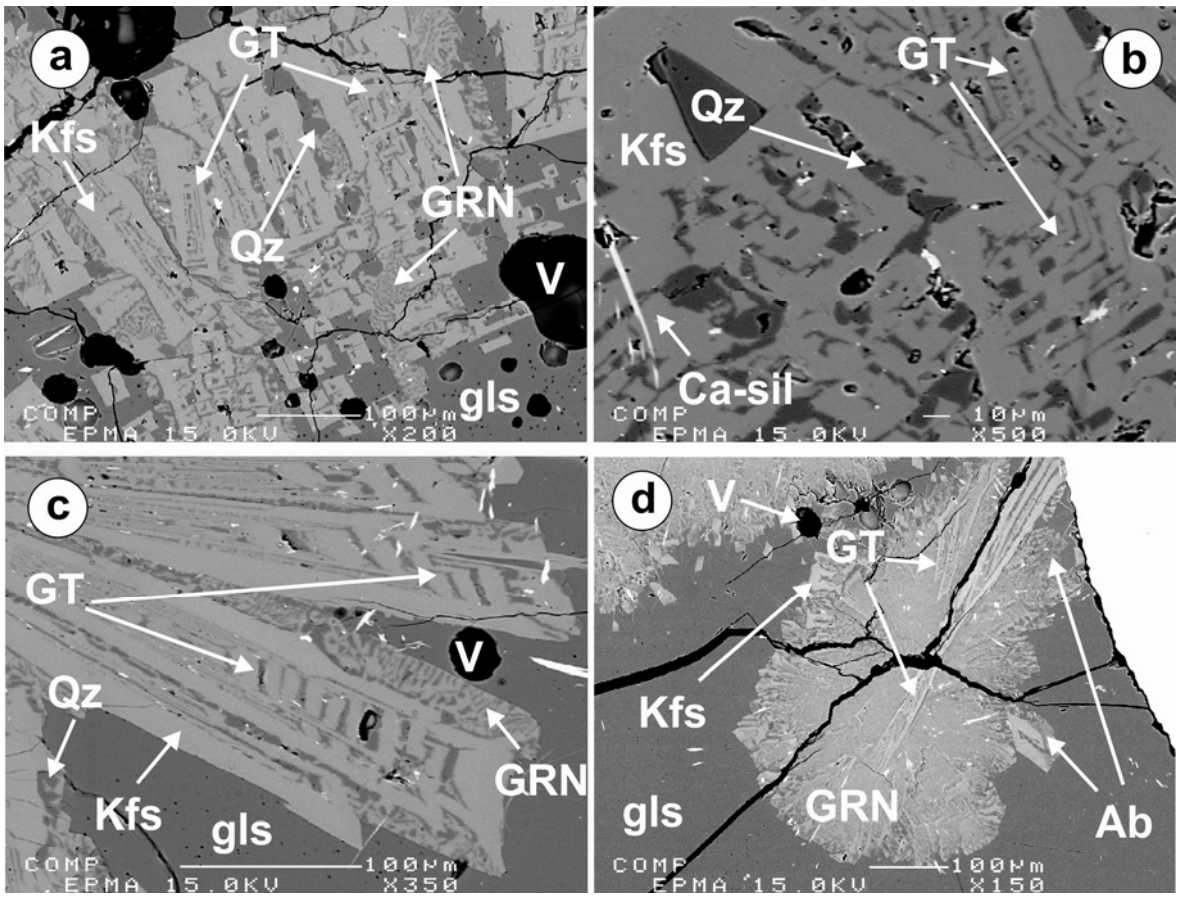

Figure 5

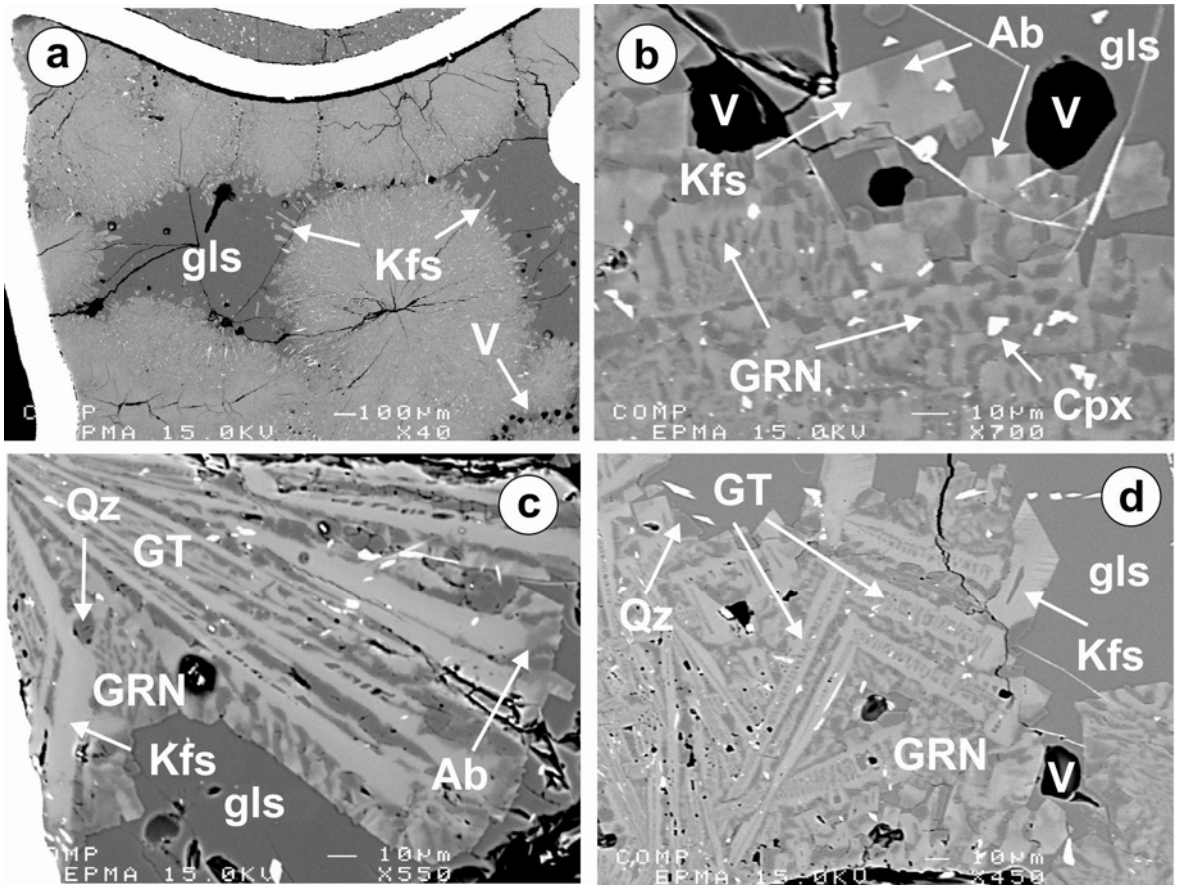

Figure 6

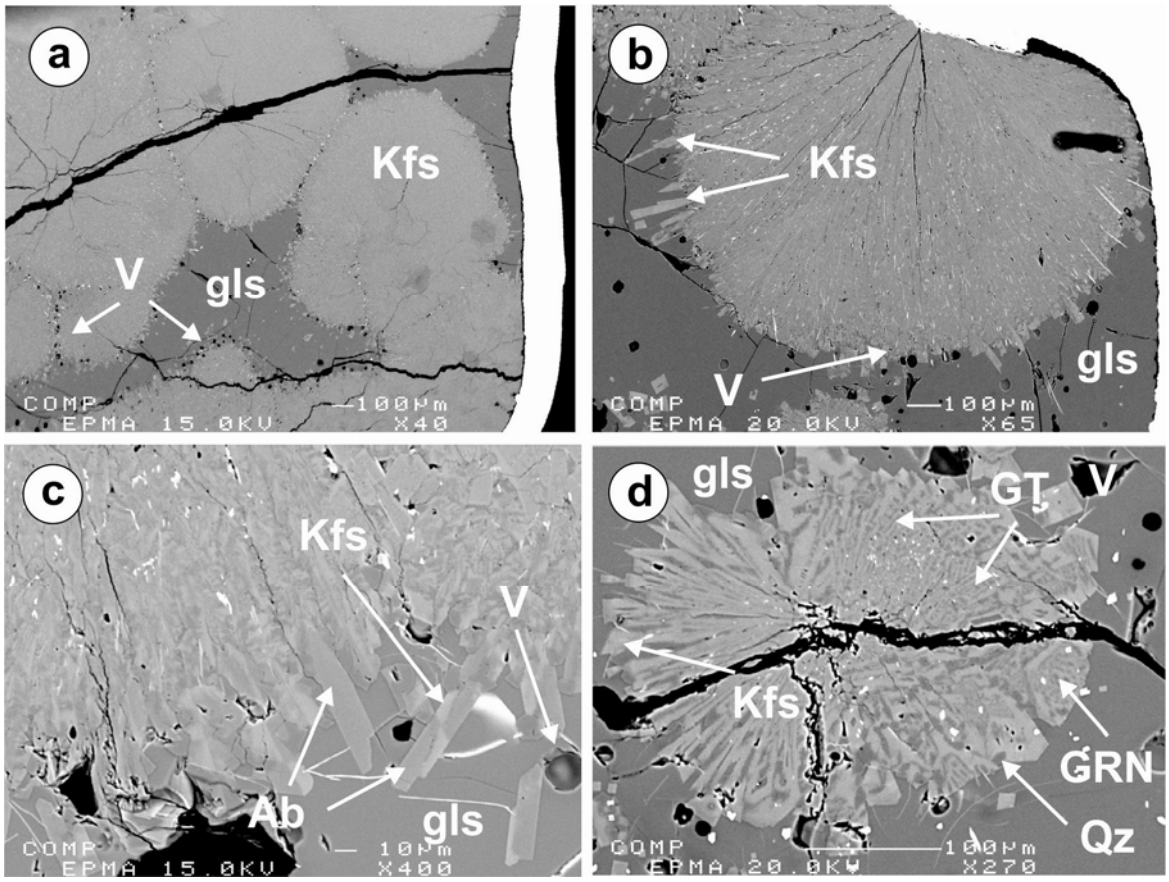

Figure 7

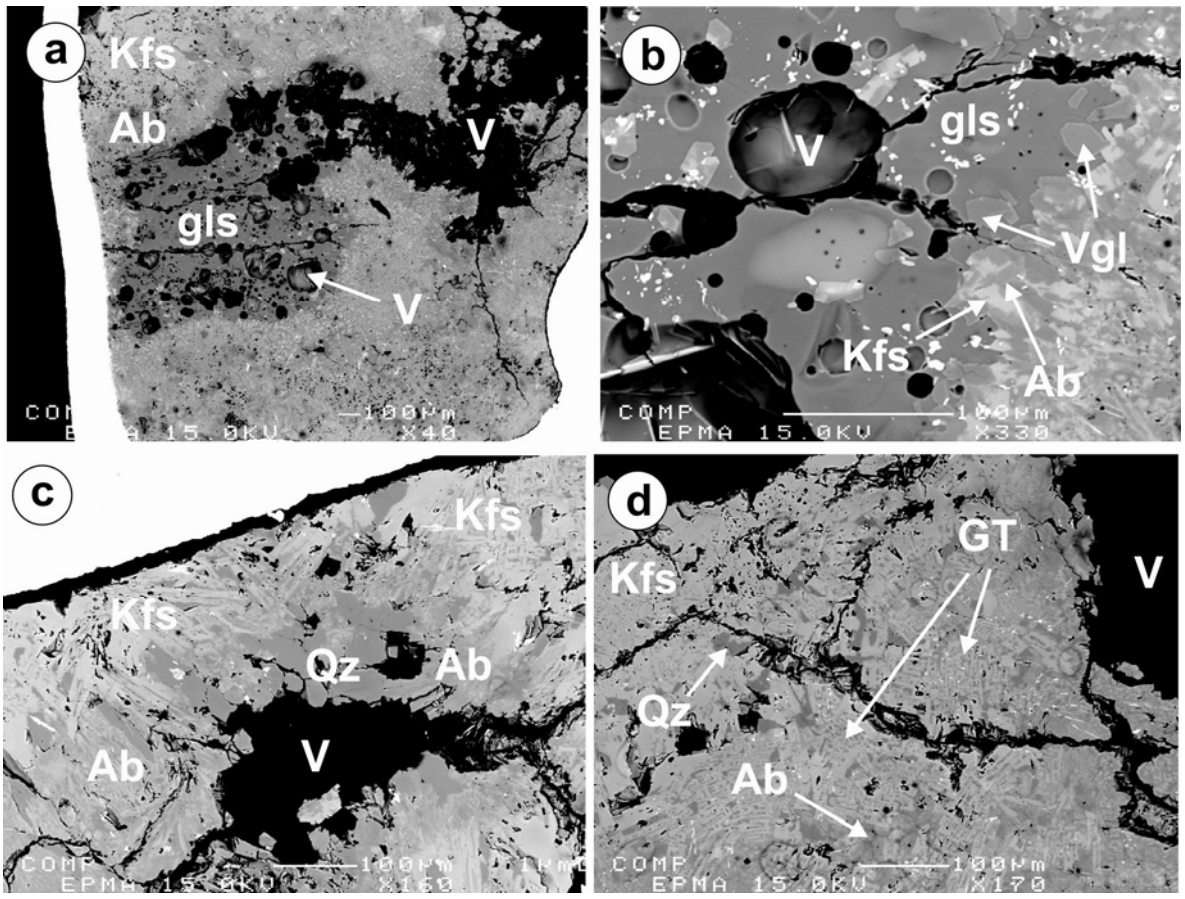

Figure 8

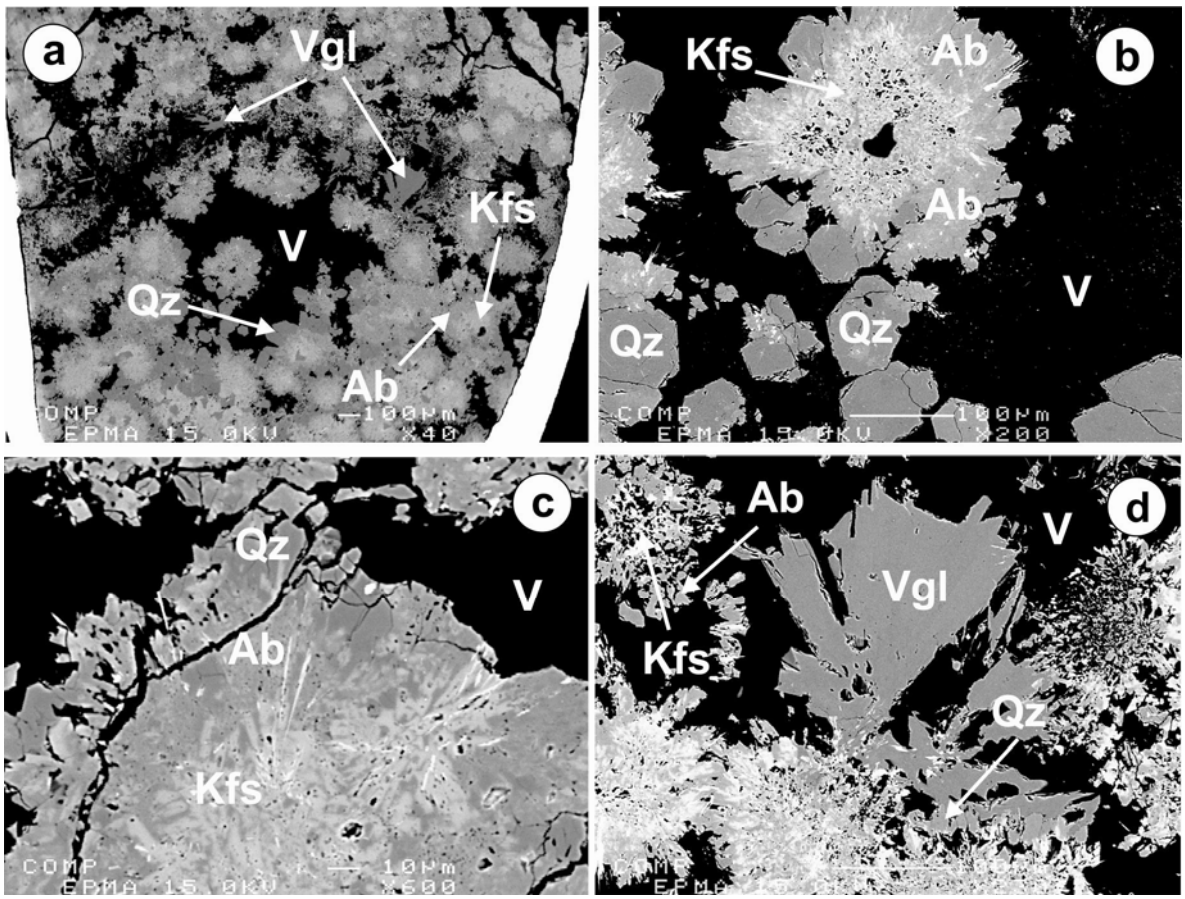

Figure 9

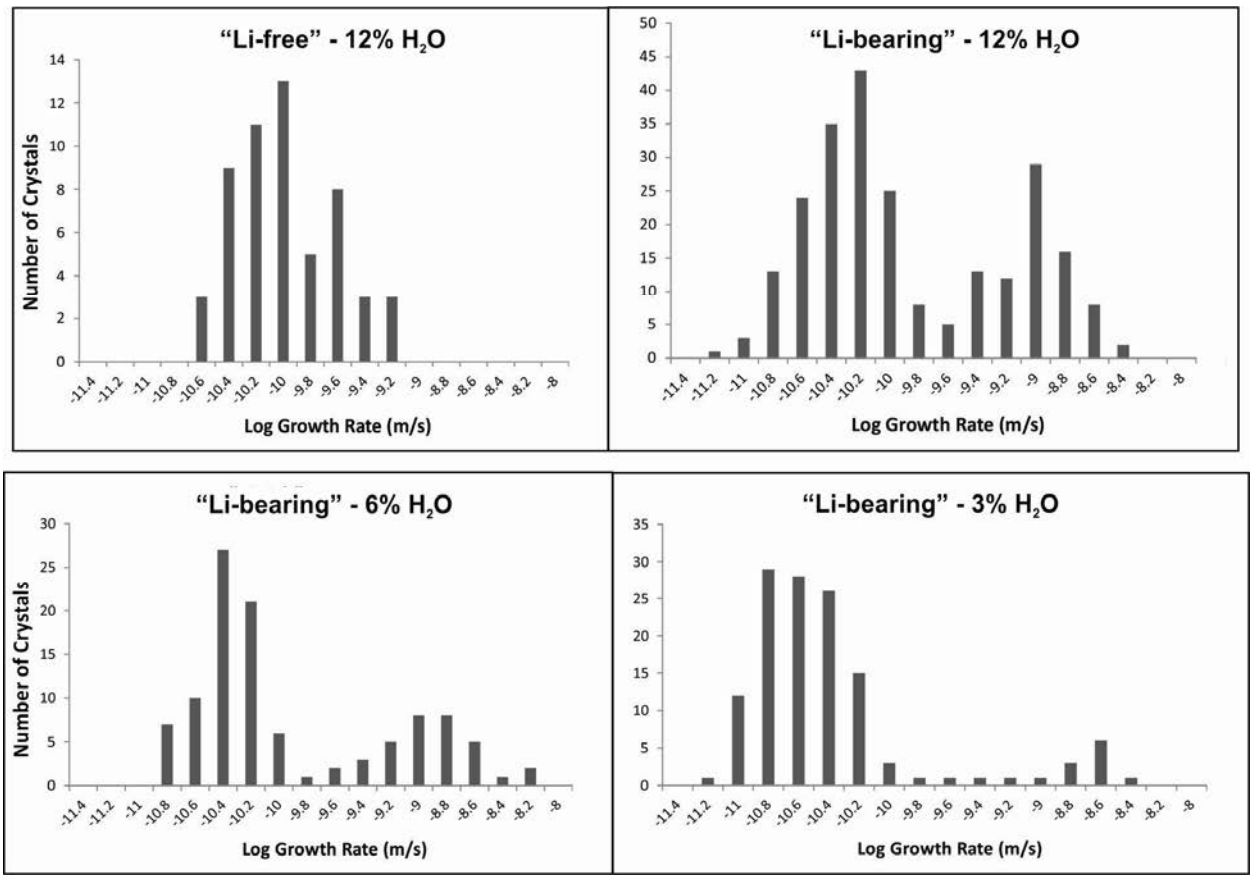

Figure 10

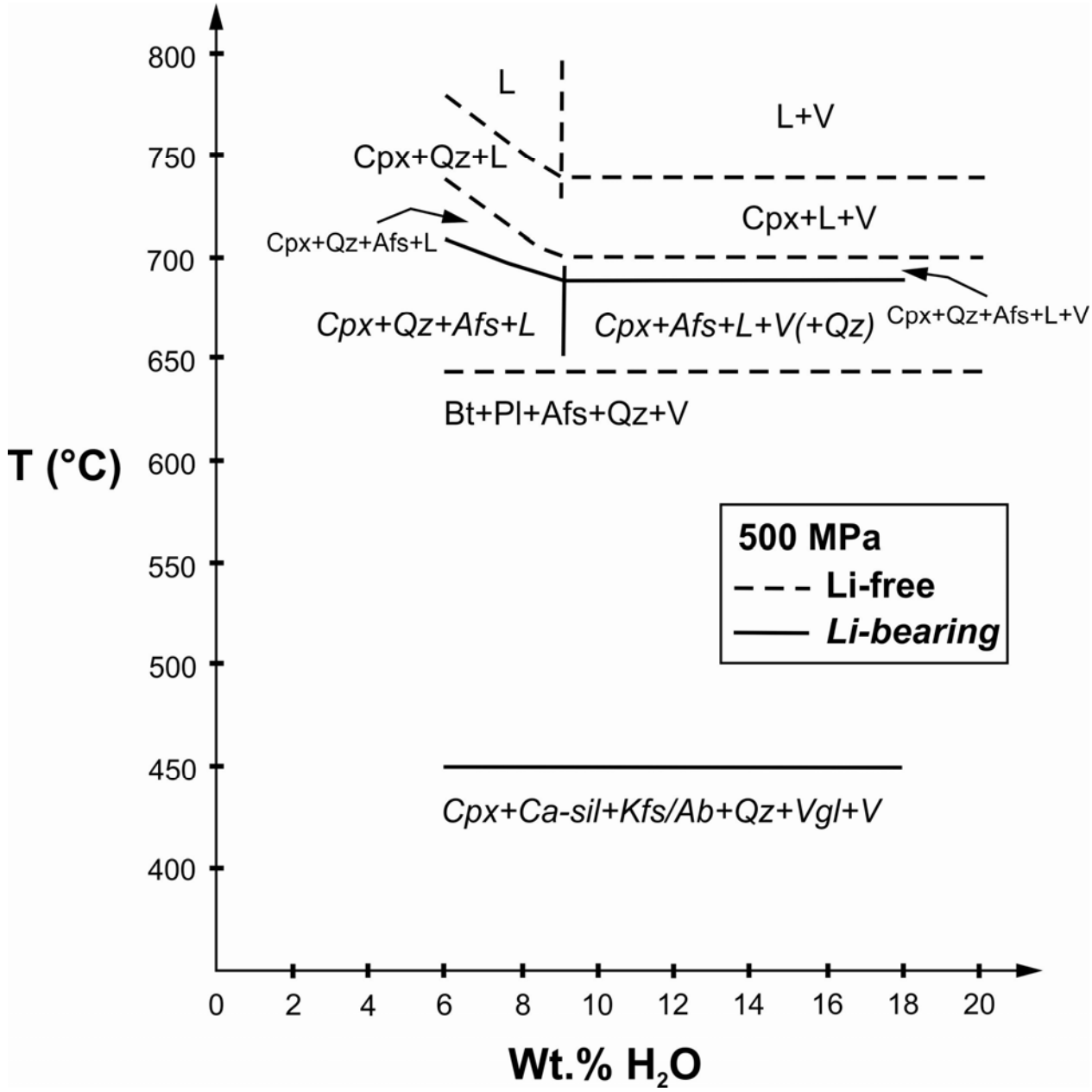

Figure 11

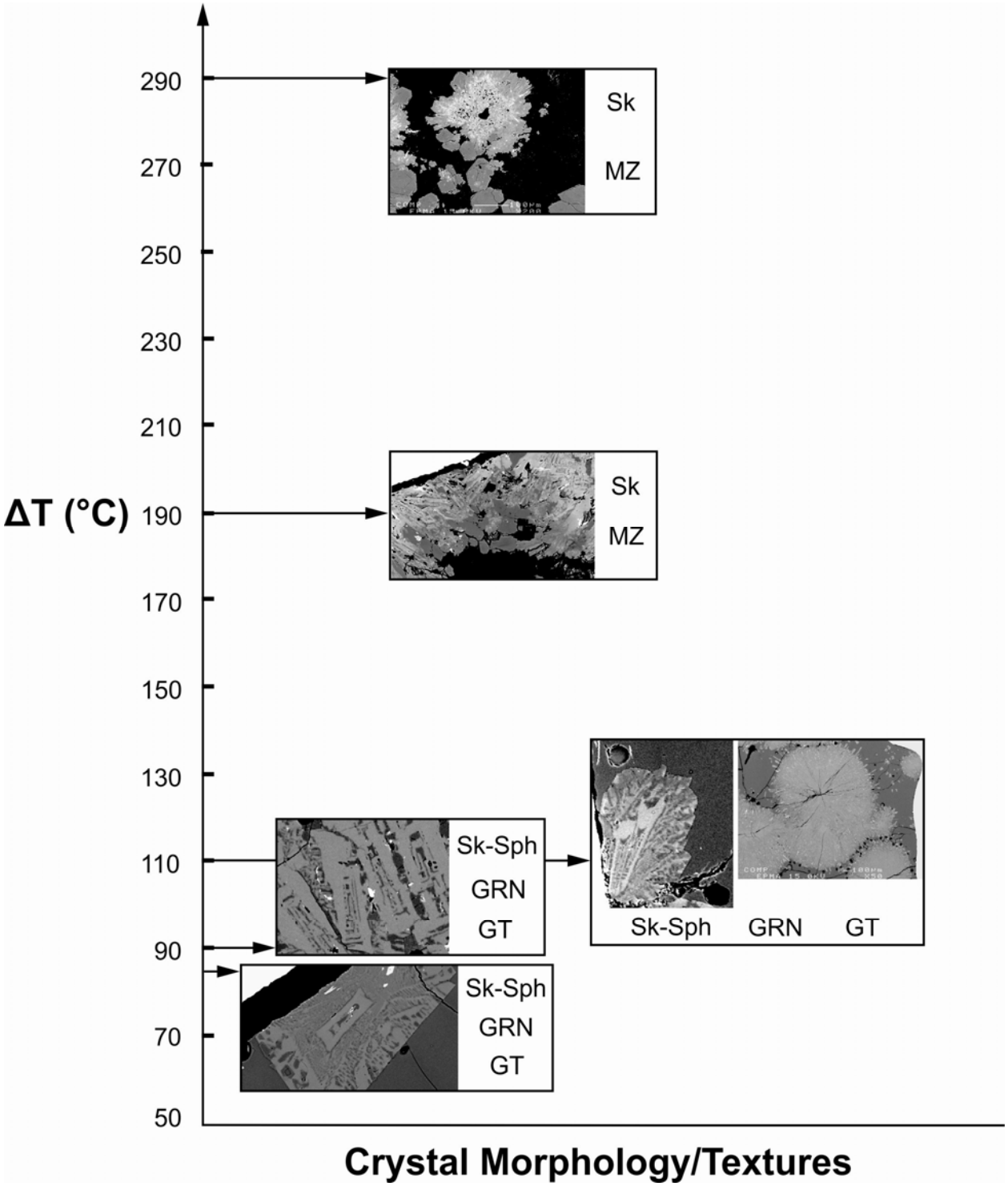

Figure 12

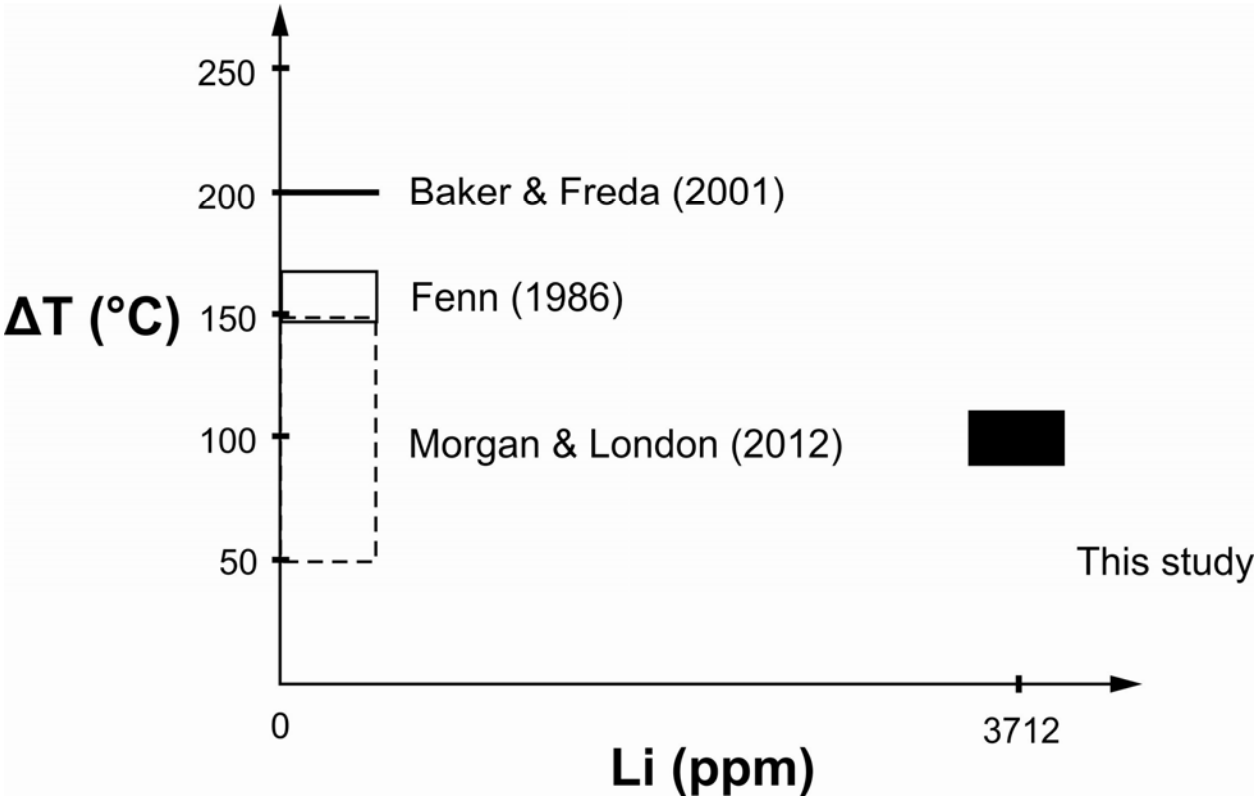

Figure 13

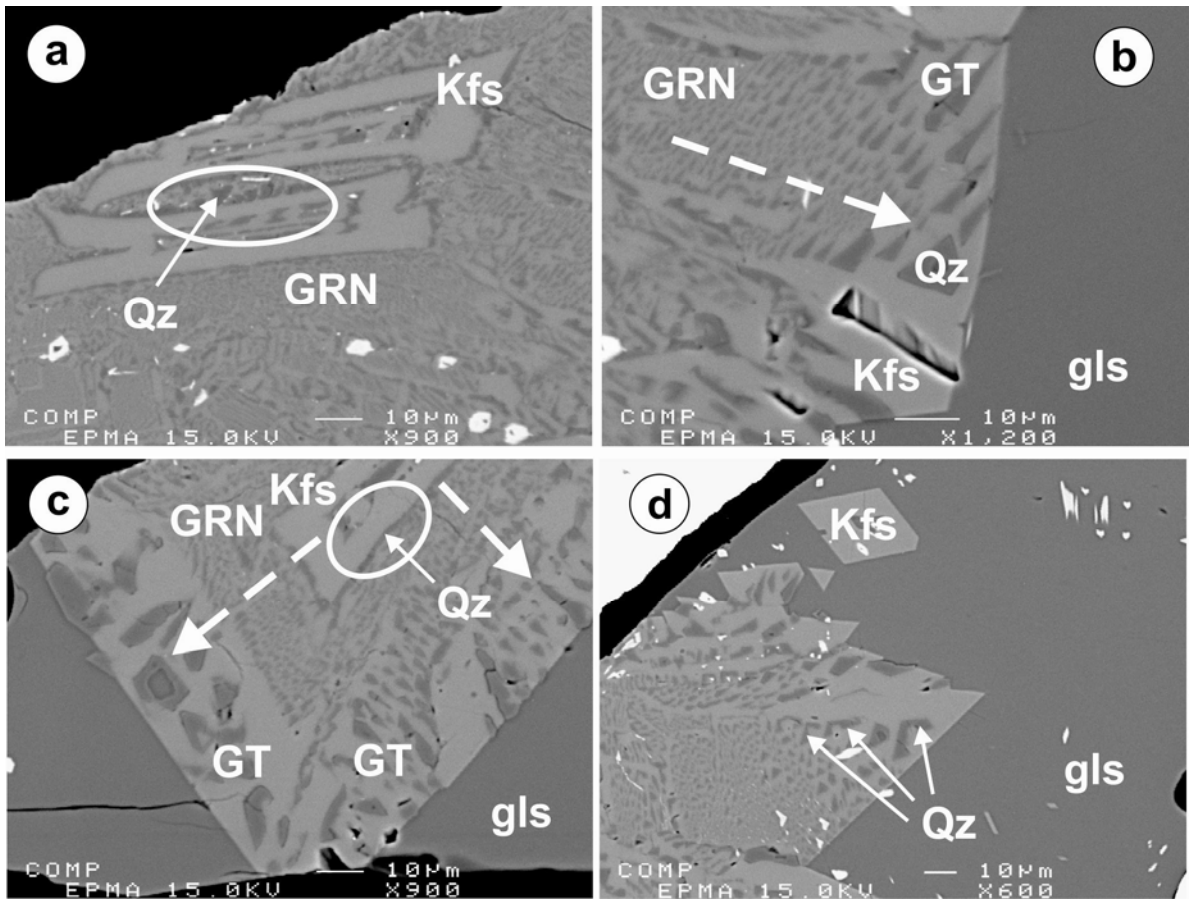

Figure 14

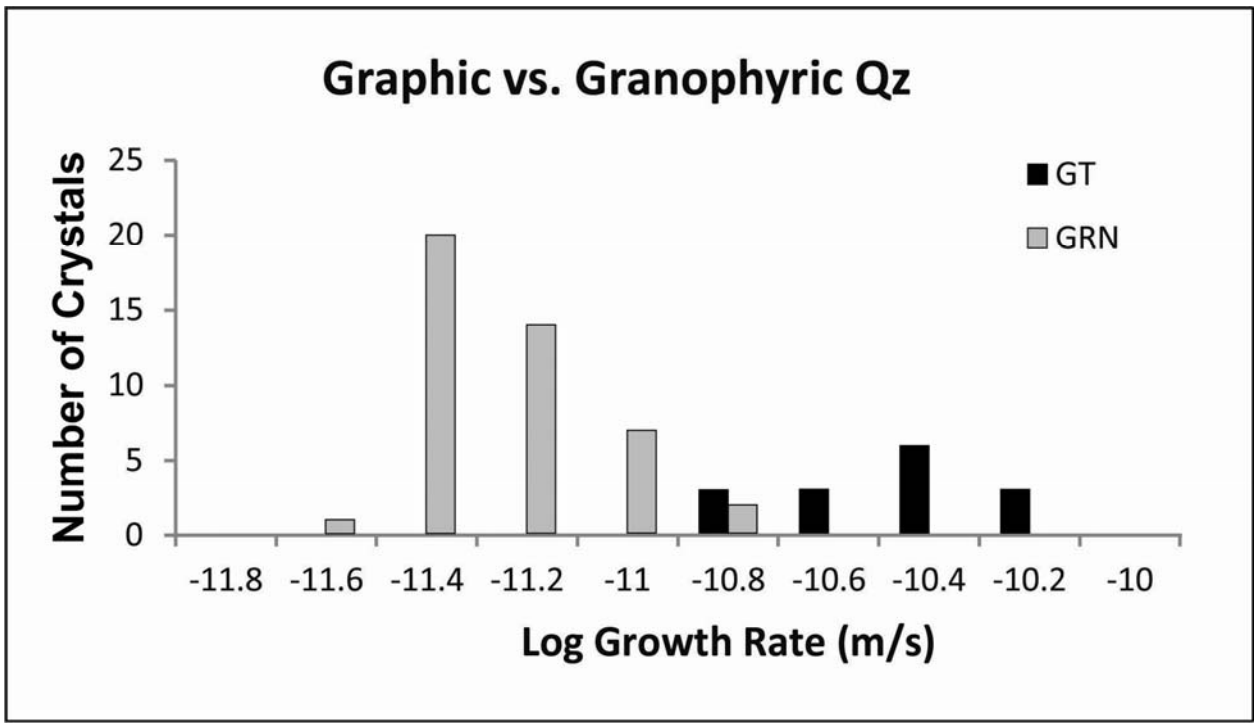

1141

1142 Figure 15

Table 1: Composition of the starting material.

Wt. % oxide	LCO[a]	Li-LCO[b] [25]
SiO_2	76.4	74.9 (3)
TiO_2	0.1	0.1 (1)
Al_2O_3	13.4	13.1 (1)
FeO	0.8	0.7 (1)
MnO	0.1	0.1 (1)
MgO	0.1	0.1 (1)
CaO	0.5	0.6 (1)
Na_2O	4.3	4.1 (1)
K_2O	4.7	5.0 (1)
P_2O_5	n.d.	b.d.
F	0	b.d.
H_2O	0.2	n.d.
Li ppm	51.9	3712 (148)
Total	100.5	99.5

[ ] Number of analyses included in the average.
( ) Standard deviation.
n.d.: not determined.
b.d.: below detection limit.

[a]EMPA data (from Baker et al. 2002), Li concentration analyzed with SIMS (from Richter et al. 2003), H_2O concentration from Harrison & Watson (1983).

[b]EMPA data obtained from this study, Li concentration analyzed with AAS.

Table 2: Experimental conditions and phases developed in the runs.

Sample	Starting material	% H_2O	Pressure (MPa)	Final Temperature (°C)	Time (h)	Phases - Textures
Li-free experiments						
PGT5	LCO	13.01	500	600	0	Glass
PGT6	LCO	11.98	500	600	0	
PGT3	LCO	13.72	500	600	50	Glass, Cpx (anhedral, subhedral), Ca-silicate (bladed), Kfs
PGT4	LCO	12.75	500	600	50	(skeletal), Qz (anhedral)
PGT1	LCO	13.82	500	600	100	Glass, Cpx (anhedral), Ca-silicate (bladed), Kfs (skeletal),
PGT2	LCO	12.87	500	600	100	Qz (anhedral)
PGT27	LCO	13.23	500	600	100	
PGT28	LCO	11.57	500	600	100	
Li-bearing experiments						
PGT39	Li-LCO	12.27	500	800	100	Glass
PGT40	Li-LCO	6.45	500	800	100	
PGT37	Li-LCO	12.97	500	750	100	Glass
PGT38	Li-LCO	7.47	500	750	100	
PGT35	Li-LCO	13.51	500	700	100	Glass
PGT36	Li-LCO	7.15	500	700	100	
PGT47	Li-LCO	13.15	500	650	100	Glass, Cpx (subhedral, euhedral), Qz (anehdral)
PGT48	Li-LCO	6.56	500	650	100	
PGT57	Li-LCO	12.23	500	625	100	Glass, Cpx (subhedral, euhedral), Ca-silicate (bladed)
PGT58	Li-LCO	5.96	500	625	100	Glass, Cpx (subhedral, euhedral), Ca-silicate (bladed), Kfs (skeletal, tabular,spherulites), Qz (anhedral, subhedral), graphic intergrowths, granophyric intergrowths
PGT43[a]	Li-LCO	12.43	500	600	100	Glass, Cpx (subhedral, euhedral), Ca-silicate (bladed)
PGT44[a]	Li-LCO	14.14	500	600	100	
PGT45[a]	Li-LCO	8.11	500	600	100	
PGT46[a]	Li-LCO	6.56	500	600	100	
PGT13	Li-LCO	13.63	500	600	0	Glass
PGT14	Li-LCO	12.32	500	600	0	

PGT25	Li-LCO	13.20	500	600	50	Glass, Cpx (anhedral), Ca-silicate (bladed), Kfs (skeletal)
PGT26	Li-LCO	13.45	500	600	50	
PGT15	Li-LCO	12.78	500	600	100	Glass, Cpx (anhedral, subhedral), Ca-silicate (bladed),
PGT16	Li-LCO	12.52	500	600	100	Kfs/Ab (skeletal, tabular, spherulites), Qz (anhedral,
PGT33	Li-LCO	12.64	500	600	100	subhedral), graphic intergrowths, granophyric
PGT34	Li-LCO	11.78	500	600	100	intergrowths
PGT17	Li-LCO	6.46	500	600	100	Glass, Cpx (anhedral, subhedral), Ca-silicate (bladed),
PGT18	Li-LCO	6.69	500	600	100	Kfs/Ab (skeletal, tabular, spherulites), Qz (anhedral,
PGT19	Li-LCO	6.74	500	600	100	subhedral), graphic intergrowths, granophyric
PGT20	Li-LCO	6.56	500	600	100	intergrowths
PGT30	Li-LCO	3.51	500	600	100	Glass, Cpx (anhedral, subhedral), Ca-silicate (bladed),
PGT31	Li-LCO	3.44	500	600	100	Kfs/Ab (skeletal, tabular, spherulites), Qz (anhedral, subhedral), graphic intergrowths, granophyric
PGT32	Li-LCO	3.43	500	600	100	intergrowths
PGT59	Li-LCO	12.17	500	500	100	Glass, Cpx (anhedral), Ca-silicate (bladed), Kfs/Ab (skeletal, tabular, spherulites), Qz (anhedral, subhedral),
PGT60	Li-LCO	6.90	500	500	100	Vgl (anhedral, subhedral), graphic intergrowths, granophyric intergrowths
PGT51	Li-LCO	12.64	500	400	100	Cpx (anhedral), Ca-silicate (bladed), Kfs/Ab (skeletal,
PGT52	Li-LCO	12.11	500	400	100	tabular, spherulites), Qz (anhedral, subhedral), Vgl
PGT53	Li-LCO	6.63	500	400	100	(anhedral), graphic intergrowths
PGT54	Li-LCO	7.04	500	400	100	

Note: Cpx= clinopyroxene, Qz= quartz, Kfs= K-feldspar, Ab= albite, Vgl= virgilite.

[a] Experiments without crystal seeds.

Table 3: Average mineral compositions obtained from EMPA data. Li concentrations were measured with SIMS.

Wt. % oxide	1 [29] K-feldspar	2 [14] Clinopyroxene	3 [5] Ca-silicate	4 [70] K-feldspar	5 [8] Quartz	6 [11] K-feldspar	7 [5] Albite	8 [2] Virgilite
SiO_2	66.1 (8)	53.4 (4)	55.7 (1.5)	66.7 (1.8)	97.2 (5)	66.9 (1.8)	69.6 (8)	88.3 (4)
TiO_2	b.d.	1.5 (6)	b.d.	b.d.	b.d.	0.1 (2)	b.d.	b.d.
Al_2O_3	17.6 (4)	1.6 (3)	2.1 (6)	17.1 (9)	0.9 (2)	16.7 (1.4)	18.0 (9)	10.6 (4)
FeO	0.1 (1)	7.5 (1.3)	0.2 (1)	0.5 (1)	b.d.	0.7 (2)	0.4 (1)	b.d.
MnO	b.d.	3.1 (4)	2.0 (2)	b.d.	b.d.	0.1 (3)	b.d.	b.d.
MgO	b.d.	10.5 (8)	0.3 (1)	b.d.	b.d.	0.1 (2)	b.d.	b.d.
CaO	0.1 (1)	18.4 (8)	38.5 (2.6)	b.d.	b.d.	0.8 (1.6)	b.d.	b.d.
Na_2O	2.2 (1)	2.4 (2)	0.3 (1)	2.2 (2)	b.d.	3.5 (5)	9.0 (7)	b.d.
K_2O	13.4 (2)	0.1 (1)	0.6 (2)	13.4 (1.6)	b.d.	10.8 (1.4)	2.6 (7)	b.d.
Li ppm	7 (3.7)[a]			181 (34.7)[b]	14[c]			9356 (3519)[d]
Total	99.5	98.5	99.7	99.9	98.1	99.5	99.6	100.9
Cations based on number of oxygens per formula unit								
	8 O pfu	6 O pfu	58 O pfu	8 O pfu	2 O pfu	8 O pfu	8 O pfu	6 O pfu
Si	3.033	2.022	20.280	3.051	0.991	3.053	3.061	2.657
Ti	0.001	0.042	0.009	0.001	0.000	0.003	0.001	0.000
Al	0.953	0.070	0.904	0.923	0.011	0.896	0.934	0.375
Fe	0.005	0.236	0.052	0.020	0.000	0.027	0.016	0.001
Mn	0.000	0.100	0.612	0.001	0.000	0.004	0.000	0.000
Mg	0.000	0.594	0.140	0.000	0.000	0.004	0.000	0.000
Ca	0.007	0.748	15.028	0.001	0.000	0.038	0.002	0.000
Na	0.197	0.172	0.176	0.191	0.000	0.306	0.767	0.000
K	0.783	0.005	0.291	0.783	0.001	0.632	0.148	0.001
Li	0.000			0.007	0.000			0.244

[ ] Number of analyses included in the average.

( ) Standard deviation.

b.d.: below detection limit.

[a]Based on 2 analyses.

[b,e]Based on 5 analyses.

[c]Based on 1 analysis.

[d]Based on 3 analyses.

1 K-feldspar: "Li-free" samples, 12% H_2O, 500 MPa, 600 °C, 100 h (PGT 28).

2 Aegirine-augite: "Li-bearing" samples, 6-12% H_2O, 500 MPa, 625 °C, 100 h. Crystals too thin for SIMS (PGT 57).

3 Ca-silicate: "Li-bearing" samples, 6-12% H_2O, 500 MPa, 625 °C, 100 h. Crystals too thin for SIMS (PGT 57).

4 K-feldspar: "Li-bearing" samples, 12% H_2O, 500 MPa, 600 °C, 100 h (PGT 15, 16).

5 Quartz: "Li-bearing" samples, 12% H_2O, 500 MPa, 600 °C, 100 h (PGT 15).

6 K-feldspar: "Li-bearing" samples, 6% H_2O, 500 MPa, 600 °C, 100 h. Crystals too thin for SIMS (PGT 17, 19).

7 Albite: "Li-bearing" samples, 6% H_2O, 500 MPa, 600 °C, 100 h. Crystals too thin for SIMS (PGT 19).

8 Virgilite: "Li-bearing" samples, 12% H_2O, 500 MPa, 500 °C, 100 h (PGT 59).

9 Virgilite: "Li-bearing" samples, 12% H_2O, 500 MPa, 400 °C, 100 h (PGT 52).

9 [16]
Virgilite
79.8 (5)
b.d.
15.4 (8)
0.1 (3)
b.d.
b.d.
b.d.
b.d.
b.d.
13215 (3743)[e]
98.1

6 O pfu
2.484
0.001
0.564
0.004
0.000
0.001
0.001
0.000
0.002
0.356

Table 4: Average glass compositions obtained from EMPA data. Li concentrations were measured with SIMS.

Wt. % oxide	1 [81]	2 [84]	3 [55]	4 [39]	5 [4]
SiO_2	66.8 (1.3)	66.9 (5)	67.3 (5)	67.9 (5)	72.9 (1.0)
TiO_2	0.1 (1)	0.1 (1)	0.1 (1)	0.1 (1)	0.1 (1)
Al_2O_3	12.0 (5)	12.3 (3)	11.9 (2)	11.5 (3)	12.5 (1)
FeO	0.6 (2)	0.6 (1)	0.6 (1)	0.8 (1)	0.4 (2)
MnO	0.1 (1)	0.1 (1)	0.1 (1)	0.1 (1)	0.1 (1)
MgO	0.1 (1)	0.1 (1)	0.1 (1)	0.1 (1)	b.d.
CaO	0.2 (1)	0.2 (1)	0.2 (3)	0.1 (1)	0.2 (1)
Na_2O	3.7 (2)	4.1 (2)	4.1 (3)	3.5 (1)	1.0 (1)
K_2O	4.5 (1)	3.2 (3)	2.8 (1)	2.7 (2)	1.1 (1)
F	b.d.	b.d.	b.d.	b.d.	b.d.
Li ppm	22 (7)[a]	3324 (331)[b]	6587 (745)[c]	12052 (982)[d]	5927 (1447)[e]
Total	88.1	88.3	88.6	89.5	89.6

[ ] Number of analyses included in the average.

( ) Standard deviation.

b.d.: below detection limit.

[a]Based on 2 analyses.

[b]Based on 10 analyses.

[c,d]Based on 4 analyses.

[e]Based on 3 analyses.

1 Glass: "Li-free" samples, 12% H_2O, 500 MPa, 600 °C, 100 h (PGT 28).

2 Glass: "Li-bearing" samples, 12% H_2O, 500 MPa, 600 °C, 100 h (PGT 15, 33, 34).

3 Glass: "Li-bearing" samples, 6% H_2O, 500 MPa, 600 °C, 100 h (PGT 19).

4 Glass: "Li-bearing" samples, 3% H_2O, 500 MPa, 600 °C, 100 h (PGT 30).

5 Glass: "Li-bearing" samples, 12% H_2O, 500 MPa, 500 °C, 100 h (PGT 59).